

1
2
3
4
5
6
7
8

This manuscript has been submitted for publication in *Basin Research*, has undergone one round of peer-review, but has **NOT** been accepted as it is undergoing further peer-review. Subsequent versions of the manuscript may differ from this one. If accepted, the final, published version of this manuscript will be available via a link on this webpage. Please feel free to contact the corresponding author with questions and/or feedback.

9 **Inverting passive margin stratigraphy for marine sediment**
10 **transport dynamics over geologic time**

11 **Charles M. Shobe^{1,2}, Jean Braun^{2,3}, Xiaoping Yuan^{2,4}, Benjamin Campforts^{2,5}, Boris**
12 **Gailleton², Guillaume Baby^{6,7}, François Guillocheau⁶, and Cécile Robin⁶**

13 *¹Department of Geology and Geography, West Virginia University, Morgantown, WV, USA*

14 *²Helmholtz Centre Potsdam, GFZ German Research Centre for Geosciences, Potsdam, Germany*

15 *³Institute of Geosciences, University of Potsdam, Potsdam, Germany*

16 *⁴Hubei Key Laboratory of Critical Zone Evolution, School of Earth Sciences, China University*
17 *of Geosciences, Wuhan, China*

18 *⁵Community Surface Dynamics Modeling System, Boulder, CO, USA*

19 *⁶Géosciences Rennes, Université de Rennes, CNRS, UMR 6118, 35000 Rennes, France*

20 *⁷Physical Science and Engineering Division, King Abdullah University of Science and*
21 *Technology, Thuwal, Saudi Arabia*

22

23 CMS (*corresponding author): charles.shobe@mail.wvu.edu

24 JB: jbraun@gfz-potsdam.de

25 XY: xyuan@gfz-potsdam.de

26 BC: benjamin.campforts@colorado.edu

27 BG: boris.gailleton@gfz-potsdam.de

28 GB: baby.guillaume@gmail.com

29 FG: francois.guillocheau@univ-rennes1.fr

30 CR: cecile.robin@univ-rennes1.fr

31 **Inverting passive margin stratigraphy for marine sediment**
32 **transport dynamics over geologic time**

33 **Charles M. Shobe^{1,2}, Jean Braun^{2,3}, Xiaoping Yuan^{2,4}, Benjamin Campforts^{2,5}, Boris**
34 **Gailleton², Guillaume Baby^{6,7}, François Guillocheau⁶, and Cécile Robin⁶**

35 *¹Department of Geology and Geography, West Virginia University, Morgantown, WV, USA*

36 *²Helmholtz Centre Potsdam, GFZ German Research Centre for Geosciences, Potsdam, Germany*

37 *³Institute of Geosciences, University of Potsdam, Potsdam, Germany*

38 *⁴Hubei Key Laboratory of Critical Zone Evolution, School of Earth Sciences, China University*
39 *of Geosciences, Wuhan, China*

40 *⁵Community Surface Dynamics Modeling System, Boulder, CO, USA*

41 *⁶Géosciences Rennes, Université de Rennes, CNRS, UMR 6118, 35000 Rennes, France*

42 *⁷Physical Science and Engineering Division, King Abdullah University of Science and*
43 *Technology, Thuwal, Saudi Arabia*

44

45 **HIGHLIGHTS**

- 46 • We compare two, 2-D stratigraphic forward models against observed marine stratigraphy.
- 47 • One model uses purely local transport dynamics while one incorporates nonlocal
- 48 transport.
- 49 • The model incorporating nonlocal transport processes produces the better fit to the data.
- 50 • Nonlocal, momentum-driven transport processes produce diagnostic stratigraphy.
- 51 • Inferring past terrestrial landscape dynamics from stratigraphy may require nonlocal
- 52 models.

53

54 **ABSTRACT**

55 Passive margin stratigraphy contains time-integrated records of landscapes that have long
56 since vanished. Quantitatively reading the stratigraphic record using coupled landscape evolution
57 and stratigraphic forward models (SFMs) is a promising approach to extracting information
58 about landscape history. However, there is no consensus about the optimal form of simple SFMs
59 because there has been a lack of direct tests against observed stratigraphy in well constrained test
60 cases. Specifically, the extent to which SFM behavior over geologic space and time scales should
61 be governed by local (downslope sediment flux depends only on local slope) versus nonlocal
62 (sediment flux depends on factors other than local slope, such as the history of slopes
63 experienced along a transport pathway) processes is currently unclear. Here we develop a
64 nonlocal, nonlinear SFM that incorporates slope bypass and long-distance sediment transport,
65 both of which have been previously identified as important model components but not
66 thoroughly tested. Our model collapses to the local, linear model under certain parameterizations
67 such that best-fit parameter values can indicate optimal model structure. Comparing 2-D
68 implementations of both models against seven detailed seismic sections from the Southeast
69 Atlantic Margin, we invert the stratigraphic data for best-fit model parameter values and
70 demonstrate that best-fit parameterizations are not compatible with the local, linear diffusion
71 model. Fitting observed stratigraphy requires parameter values consistent with important
72 contributions from slope bypass and long-distance transport processes. The nonlocal, nonlinear
73 model yields improved fits to the data regardless of whether the model is compared against only
74 the modern bathymetric surface or the full set of seismic reflectors identified in the data. Results
75 suggest that processes of sediment bypass and long-distance transport are required to model

76 realistic passive margin stratigraphy, and are therefore important to consider when inverting the
77 stratigraphic record to infer past perturbations to source regions.

78

79 **INTRODUCTION**

80 Reconstructing landscape evolution trajectories—and the environmental boundary conditions
81 that governed them—from the geologic past is a key goal in geomorphology. Such
82 reconstructions are challenging because erosion processes continually destroy past topography,
83 leaving only minor traces of ancient landscapes (e.g., river terraces; Molnar et al., 1994; Schanz
84 et al., 2018; Yuan et al., 2022) from which to deduce past landscape boundary conditions.
85 Fortunately, every source has its sink; all sediment eroded from a terrestrial drainage basin must
86 go somewhere. The sedimentary record, in regions where it is preserved and where there exists
87 plausible long-term connectivity between source and sink, therefore represents our best hope of
88 inferring time-resolved records of landscape change and its tectonic and climatic drivers with
89 reasonable accuracy and precision. One geologic setting with particularly high potential for the
90 preservation of relatively complete records of terrestrial erosion is marine passive margin basins,
91 which contain Earth’s most complete archives of sediment sourced from adjacent, eroding
92 terrestrial environments (e.g., Steckler et al., 1988; Allen and Allen, 2013).

93 Passive margin stratigraphy can, under the right conditions, be used to reconstruct past
94 tectonic and climatic perturbations to Earth’s surface (e.g., Poag and Sevon, 1989; Poag, 1992;
95 Pazzaglia and Brandon, 1996; Baby et al., 2018; Ding et al., 2019a). While the stratigraphic
96 record can suffer from signal buffering, stratigraphic incompleteness, and signal shredding (e.g.,
97 Sadler, 1981; Jerolmack and Paola, 2010; Straub et al., 2020), the variability that leads to these
98 effects is thought to yield average behavior that can be predicted at passive margin evolution

99 timescales (tens to hundreds of Ma). Passive margin stratigraphy may reflect large-scale, long-
100 lasting perturbations to landscapes provided that those perturbations have amplitudes and
101 durations that exceed the background level of “noise” in the sedimentary system (Straub et al.,
102 2020). Historically, efforts to read the stratigraphic record of passive margins have focused on
103 the study of sediment thickness, volume, texture, lithological/mineralogical makeup, and
104 chemistry, yielding interpretations about past terrestrial erosion dynamics (e.g., Poag and Sevon,
105 1989). As numerical stratigraphic forward models (SFMs) became more common (e.g., Steckler
106 et al., 1993; 1996; Syvitski and Hutton, 2001; Granjeon and Joseph, 1999; Burgess et al., 2006;
107 Burgess, 2012), stratigraphic modelers began to use inverse techniques to extract environmental
108 forcing information from forward simulation of the stratigraphic record (e.g., Lessenger and
109 Cross, 1996; Cross and Lessenger, 1999; Bornholdt and Westphal, 1998; Bornholdt et al., 1999;
110 Imhof and Sharma, 2006; 2007; Olivene et al., 2014; Zhang et al., 2021). The great potential of
111 that record for revealing past landscape evolution has led to efforts to couple landscape evolution
112 models (LEMs) and SFMs (e.g., Granjeon and Joseph, 1999; Salles and Hardiman, 2016; Salles
113 et al., 2018; Ding et al., 2019a,b; Yuan et al., 2019a, Salles, 2019; Zhang et al., 2020) to build
114 full source-to-sink models, and in some cases to use large ensembles of those models to directly
115 invert observed stratigraphy for terrestrial erosion dynamics (e.g., Yuan et al., 2019a). The idea
116 underpinning such inversions is that misfit between observed and modeled stratigraphy can be
117 minimized to reveal best-fit values for relevant forcing parameters such as rock uplift rate,
118 assuming that the model is an accurate representation of erosion, transport, and deposition
119 processes integrated over geologic time.

120 Many previous efforts focused on margin spatial scales and ~100 Ma timescales have used an
121 approach in which marine sediment transport is conceptualized as being linearly dependent on

122 local bathymetric slope, which when combined with mass conservation yields a linear-diffusion-
123 like model (e.g., Moretti and Turcotte, 1985; Kenyon and Turcotte, 1985; Rivenaes, 1992; 1997;
124 Ross et al., 1994; Paola, 2000; Braun et al., 2013; Rouby et al., 2013; Yuan et al., 2019a; Zhang
125 et al., 2020). However, this approach might not be capable of producing large-scale stratal
126 geometries that agree with observations. In the stratigraphy of many passive margin basins, we
127 observe substantial accumulations of sediment hundreds of kilometers from shore on the
128 continental rise and abyssal plain that must have bypassed the higher-gradient continental slope
129 (Lowe, 1976; Syvitski et al., 1988) and then been transported long distances over negligible
130 slopes on the basin floor (Wynn et al., 2002; Talling et al., 2012, Luchi et al., 2018; Hereema et
131 al., 2020).

132 The sole dependence of sediment flux on local slope neglects both sediment transport over
133 very low slopes and the potential influence of nonlocal transport processes, or those processes
134 for which the distribution of sediment travel distances is heavy-tailed such that some sediment
135 moves long distances relative to the scale of the model grid (e.g., Fofoula-Georgiou et al.,
136 2010). Transport processes are especially likely to deviate from local-slope-dependent behavior
137 when sediment particles are fine enough to be suspended in the water column as observed in
138 turbidity currents and other marine mass flows (e.g., Parker et al., 1986; Mohrig et al., 1998). In
139 a nonlocal conceptualization of downslope sediment transport, erosion or deposition at a point
140 has some dependence on surface slope elsewhere (Furbish and Roering, 2013; Doane et al.,
141 2018). Nonlocal processes like sediment plumes from river mouths, turbidity currents, marine
142 landslides, and debris flows are responsible for much of the long-distance transport observed
143 along passive margins and are therefore relevant for any model that seeks to simulate passive
144 margin stratigraphy. Such processes and deposits may not be fully consistent with the

145 assumptions or predictions of local, linear transport models because they may require nonlocal
146 and/or nonlinear conceptualizations of sediment transport dynamics.

147 Stratigraphic forward modeling studies have moved beyond local, linear diffusion models to
148 incorporate nonlocal sediment transport dynamics with varying degrees of complexity (e.g.,
149 Granjeon and Joseph, 1999; Syvitski and Hutton, 2001; Sømme et al., 2009; Granjeon, 2014;
150 Harris et al., 2016; Ding et al., 2019a, Falivene et al., 2019). However, the extent to which
151 nonlocality should play a role in large-scale SFMs remains unclear, as previous comparisons
152 between local and nonlocal transport formulations have not always revealed clear differences
153 (Granjeon, 2014), and few studies have focused on the deep, distal portions of margins where
154 nonlocal process dynamics may contribute most to shaping margin form. While substantial effort
155 has been devoted to parameterizing large-scale terrestrial landscape evolution models (e.g.,
156 Guerit et al., 2019; Yanites et al., 2018; Barnhart et al., 2019; Barnhart et al., 2020a,b,c) to test
157 how well they predict landscape form (e.g., van der Beek and Bishop, 2003; Valla et al., 2010;
158 DiBiase and Whipple, 2011; Hobbey et al., 2011; Barnhart et al., 2020b), the same is not true of
159 SFMs. The mathematical form of simple, long-term/large-scale seascape evolution models that
160 best represents the development of passive margin stratigraphy is currently an open question.

161 Here we test a generalized two-dimensional (2-D) SFM that moves beyond local, linear
162 diffusion by incorporating, as suggested by previous work, sediment transport dynamics that
163 allow sediment to bypass steep slopes and travel beyond the base of the continental slope. Our
164 approach is intended not to simulate such processes explicitly, but to model their integrated
165 effects over geologic time. We test the relative applicability of this nonlocal model and the local,
166 linear model by quantitative comparison against seismic stratigraphic data from well-studied
167 passive margin basins along the Southeast Atlantic Margin (SAM), southern Africa. Results from

168 model-data comparison indicate that, at least over ~100 Ma timescales, passive margin seascape
169 evolution and the development of marine stratigraphy are most consistent with a model that
170 incorporates nonlocal and nonlinear transport dynamics. This indicates that passive margin
171 evolution may be dominated by nonlocal, nonlinear sediment transport processes that may be
172 critical ingredients in models used to invert passive margin stratigraphy for past environmental
173 forcings.

174

175 **MODELING SEASCAPE EVOLUTION OVER GEOLOGIC TIME**

176

177 **Model Dimensionality**

178 Below, we cast the local, linear and nonlocal, nonlinear models in a form that, by
179 convention in the SFM literature (and in contrast to conventions governing LEMs), is referred to
180 as 2-D because any point in the model grid can be uniquely specified by a horizontal and a
181 vertical coordinate. This choice is essential to keep our model evaluation exercise tractable and
182 interpretable given the available stratigraphic data, but it is important to note that fully 3-D SFMs
183 are routinely used (e.g., Falivene et al., 2020; Zhang et al., 2021) and in some cases allow
184 development of preferential nonlocal sediment transport pathways (e.g., submarine canyons) that
185 the models we test here can only claim to represent on average over geologic time (e.g.,
186 Granjeon, 2014).

187

188 **The Local, Linear Diffusion Model**

189 The simplest and longest-standing approach to modeling seascape evolution (and therefore
190 the way, by tracking the bathymetric surface through time, of modeling marine stratigraphy) is to

191 use an analogy to the heat equation that yields a linear diffusion equation where elevation z is the
192 variable “diffusing” over time and where the gradient driving diffusion is the bathymetric slope
193 $\frac{\partial z}{\partial x}$ (Kenyon and Turcotte, 1985; Ross et al., 1994). The downslope sediment flux per unit contour
194 length q_s goes linearly with local slope ($S = \frac{\partial z}{\partial x}$ for simplicity):

$$195 \quad q_s = -K_d S, \quad (1)$$

196 and the divergence of sediment flux sets the rate of bathymetric change:

$$197 \quad \frac{\partial z}{\partial t} = -\frac{\partial q_s}{\partial x} = K_d \frac{\partial^2 z}{\partial x^2}. \quad (2)$$

198 Here K_d [L^2/T] is a transport coefficient that governs the rate of bathymetric diffusion. The key
199 assumption in this approach is that downslope sediment flux goes linearly with the local slope,
200 such that no variables beyond K_d and bathymetry influence the rate of seascape evolution.

201 There is no clear physical basis for such a slope-dependent diffusion equation at low slopes
202 (i.e., on the continental shelf) and shallow water depths (see Paola, 2000 for a review), and an *ad*
203 *hoc* solution has been to assert that the diffusion rate constant declines with water depth d (e.g.,
204 Kaufman et al., 1992; van Balen et al., 1995) as wave- and storm-driven bed shear stresses are
205 reduced:

$$206 \quad K_d(d) = K_{d_0} e^{-d/d_*}. \quad (3)$$

207 Here K_{d_0} is the diffusion rate constant at the water surface ($d = 0$) and d_* is the e-folding depth
208 scale that governs the decline in K_d with depth below the water surface. When d_* is small
209 relative to the total basin depth (i.e., when there are substantial declines in sediment transport
210 efficiency with depth), the linear diffusion approach yields morphologies analogous to
211 continental shelves, shelf breaks, and steeper continental slopes. Similar results are achieved by
212 asserting that terrestrial sediment fluxes deposit at a fixed slope when they reach the shoreline

213 and then become subject to marine sediment transport by linear diffusion (Yuan et al., 2019a).
214 Linear diffusion models, with or without modifications in the shallow environment, deliver little
215 sediment beyond the base of the continental slope because the governing equation asserts that the
216 downslope sediment flux approaches zero as the local slope approaches zero.

217 The inconsistency of local, linear diffusion models with observations of nonlocal transport
218 and long-distance sedimentation has long been noted (e.g., Syvitski et al., 1988), and has
219 motivated model modifications such as adding advective components of sediment transport
220 (Niedoroda et al., 1995, Pirmez et al., 1998; Thran et al., 2020), allowing sediment bypass on
221 slopes above some angle (e.g., Lowe, 1976; Syvitski et al., 1988; Ross et al., 1994; Thran et al.,
222 2020), and enforcing that only some (potentially slope-dependent) proportion of the sediment
223 flux may be deposited at any given point, with the rest being routed downslope (Ding et al.,
224 2019a, Thran et al., 2020). There are also several higher-complexity, 3-D SFMs that incorporate
225 nonlocal transport by explicitly simulating advective processes (e.g., Granjeon and Joseph, 1999;
226 Granjeon, 2014; Falivene et al., 2019). Here we generalize ideas from existing SFMs, as well as
227 recent advances from terrestrial landscape evolution modeling, into a simple SFM that
228 incorporates two key modifications to account for both transport over low slopes and nonlocal
229 transport.

230 **A Modified Seascape Evolution Model**

231 The modified model is a generalization of existing ideas for how seascape evolution
232 might deviate from the local, linear model that (1) is simple enough to be applied over basin-
233 filling timescales, (2) is parsimonious enough to allow iterative calibration of all parameters, and
234 (3) collapses under certain parameter values to the local, linear model. The model is most
235 intuitively cast in terms of a balance between the volumetric entrainment rate per unit bed area E

236 and volumetric deposition rate per unit bed area D (e.g., Beaumont et al., 1992; Kooi and
237 Beaumont, 1994; van Balen et al., 1995; Davy and Lague, 2009; Carretier et al., 2016; Shobe et
238 al., 2017; Yuan et al., 2019b; Campforts et al., 2020; Braun, 2021). The statement of mass
239 conservation that governs the change in bathymetry at a point is:

$$240 \quad \frac{\partial z}{\partial t} = -E + D . \quad (4)$$

241 This framework is convenient because both of the models we propose to compare—the
242 local, linear model and the nonlocal, nonlinear model—can be represented by altering the
243 functional forms of E and D . As shown by Carretier et al. (2016), assuming that the entrainment
244 rate is linearly proportional to the local slope S :

$$245 \quad E = K_e S , \quad (5)$$

246 that K_e is an entrainment rate constant [L/T], and that the deposition rate is the volumetric
247 sediment flux per unit width q_s over the model grid cell spacing dx :

$$248 \quad D = \frac{q_s}{dx} , \quad (6)$$

249 yields the local, linear model with behavior identical to equation 2. Its two key assumptions are
250 that sediment entrainment depends only on local slope and that the deposition rate depends only
251 on the downslope sediment flux.

252 The nonlocal, nonlinear model uses equation 5 to calculate sediment entrainment but
253 makes two key modifications to equation 6 inspired by observations from passive margin
254 depositional systems. These are intended to allow (1) a nonlinear dependence of sediment
255 transport on local slope to account for the transition to mass failures and turbidity currents at
256 higher slopes as well as sediment bypass on slopes unable to sustain further steepening beyond
257 some critical slope at which frequent failures are generated, and (2) transport of sediment over
258 negligible slopes as observed in data from deep marine deposits (e.g., Wynn et al., 2002). Our

259 modified model rests heavily on recent advances in terrestrial and marine modeling, especially
260 the framework proposed by Carretier et al. (2016) for hillslope sediment transport.

261 Carretier et al. (2016) proposed altering equation 6 to encapsulate a nonlinear dependence
262 of the deposition rate on slope such that sediment deposition declines as slope increases towards
263 some imposed threshold (e.g., Andrews and Bucknam, 1987; Roering et al., 1999), such that:

$$264 \quad D = \frac{q_s \left(1 - \left(\frac{S}{S_c}\right)^2\right)}{dx}. \quad (7)$$

265 Here S_c is the critical slope, best thought of physically as the slope at or above which no further
266 deposition can occur and all remaining sediment continues downslope. As discussed by Carretier
267 et al. (2016), this model is nonlocal in the sense that sediment supplied from upslope can
268 continue downslope if the deposition rate is insufficient to disentrain all sediment. Similar
269 approaches to sediment bypass have also been used in recent seascape evolution models (e.g.,
270 Thran et al., 2020).

271 Equation 7 has one feature that makes it less than suitable for modeling marine transport:
272 at a slope of zero, all sediment in transport is deposited. This is not a problem encountered in the
273 eroding hillslopes for which the model was developed (Carretier et al., 2016), but contradicts the
274 observed behavior of marine sediment transport processes like turbidity currents that can travel
275 hundreds of km over negligible slopes. Because our goal is to simulate the integrated effects of
276 such events over basin-filling timescales, our model must have a mechanism for transport of
277 sediment over negligible slopes.

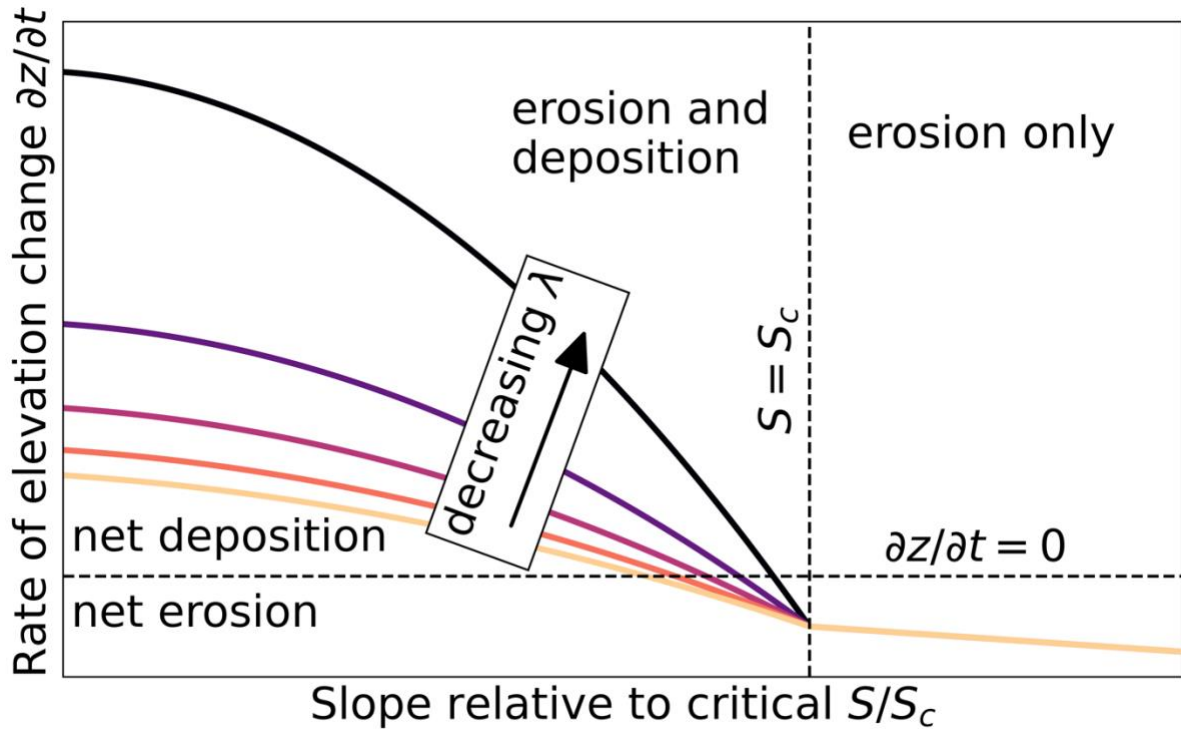
278 To allow transport of sediment over near-zero slopes, we modify Carretier et al's (2016)
279 model by adopting from Ding et al. (2019a) the idea that only some proportion of sediment in
280 transport will be deposited at any given location. We incorporate this modification by altering
281 equation 7 to:

282
$$D = \frac{q_s(1-(S/S_c)^2)}{\lambda}, \quad (8)$$

283 where λ is a sediment transport length scale that is at least the model grid cell spacing. When
284 $\lambda \gg dx$, only some small proportion of the amount of sediment in transport is deposited. The
285 rest continues in transport towards the distal portion of the margin. When $\lambda = dx$, all sediment in
286 transport is deposited. While this approach is heuristic—values of λ likely depend on grain size
287 but are not tied explicitly in our model to specific properties of the sediment or the transport
288 system—it allows the model to incorporate the general sediment transport patterns thought to
289 occur in the deep, distal portions of continental margins. Modeled sediment can travel long
290 distances down the continental slope because entrainment is linearly proportional to slope
291 (equation 5) and because deposition becomes negligible as slopes approach the critical slope of
292 non-deposition (equation 8). At the base of the continental slope, low slopes drive reduced
293 sediment entrainment rates and increased deposition rates, but the condition $\lambda \gg dx$ allows
294 continued transport across the abyssal plain in lieu of direct calculations of debris flow/turbidity
295 current transport (e.g., Parker et al., 1986). The modified model allows an approximation of
296 nonlocal transport in the sense that the amount of sediment deposited at a given distance from
297 shore depends not only on the local slope at that point but on all the points upslope that have
298 contributed sediment to—or removed it from—active transport.

299 At a point, the rate of elevation change responds to the sediment flux per unit width q_s ,
300 the entrainment coefficient K_e , the slope S relative to the critical slope of non-deposition S_c , and
301 the sediment transport length scale λ (Figure 1). For a given λ , there is a shift from net
302 deposition to net erosion as S approaches S_c as the deposition rate declines and the entrainment
303 rate increases. At a given S/S_c increasing λ causes a shift towards less deposition (or more net

304 entrainment) as more sediment remains in transport. The S/S_c at which there exists a shift from
 305 net deposition to net entrainment (i.e., a shift from positive $\frac{\partial z}{\partial t}$ to negative $\frac{\partial z}{\partial t}$) depends on λ . For
 306 $S/S_c > 1$, no deposition can occur, λ ceases to matter, and entrainment continues to scale
 307 linearly with slope.



308

309 **Figure 1: Model behavior—as shown by the rate of elevation change—as a function of $\frac{S}{S_c}$ (where $S = \frac{\partial z}{\partial x}$) and**
 310 **λ . Decreasing the transport length scale leads to increased deposition, and therefore positive changes in**
 311 **elevation, when the slope is below the slope of non-deposition. When the slope is at or above the slope of non-**
 312 **deposition, the transport length scale ceases to matter because no deposition occurs and all sediment bypasses**
 313 **the cell. The sediment entrainment rate increases linearly with slope, and deposition rate decreases**
 314 **nonlinearly with slope, leading to net erosion as slopes increase towards the slope of non-deposition. The**
 315 **erosion coefficient is held constant in this figure.**

316

317 We follow previous work (Kaufman et al., 1992; van Balen et al., 1995) in our treatment of

318 both the local, linear model and the nonlocal, nonlinear model by asserting that the erosion

319 coefficient K_e declines exponentially with water depth d below some surface value K_{e0} :

320
$$K_e(d) = K_{e0} e^{-d/d_*} . \quad (9)$$

321 This accounts for the erosive energy that may prevent the development of steep slopes close
322 to the shoreline. The complete governing equation for the commonly used linear, local model in
323 the erosion-deposition framework is found by substituting equations 5, 6, and 9 into equation 4:

$$324 \frac{\partial z}{\partial t} = -K_{e_0} e^{-d/d_*} S + \frac{q_s}{dx}. \quad (10)$$

325 The complete equation for bathymetric evolution under the nonlocal, nonlinear model is found
326 by substituting equations 5, 8, and 9 into equation 4:

$$327 \frac{\partial z}{\partial t} = -K_{e_0} e^{-d/d_*} S + \frac{q_s \left(1 - (S/S_c)^2\right)}{\lambda}. \quad (11)$$

328 Equation 10 has two parameters: the sediment entrainment coefficient at zero water depth
329 K_{e_0} [L/T] and the depth scale d_* [L] over which the entrainment coefficient declines with depth.

330 Equation 11 has two additional parameters: the slope of non-deposition S_c [-] and the sediment
331 transport length scale λ [L]. Sediment compaction due to the deposition of overburden is
332 calculated using the assumption of an exponential decay in porosity φ with depth below the
333 bathymetric surface h (e.g., Sclater and Christie, 1980; Yuan et al., 2019a):

$$334 \varphi(h) = \varphi_0 e^{-h/h_*}, \quad (12)$$

335 where φ_0 is the surface porosity and h_* is the e-folding length scale governing the decay of
336 porosity with depth. We used φ_0 and h_* values of 0.56 and 2830 m, respectively, obtained by
337 averaging the sand and clay compaction parameters of Guillocheau et al. (2012).

338 We only apply equation 11 to positive slopes (defined as sloping from the shore towards
339 the basin). For adverse slopes, we assert for simplicity that $E = 0$ and $D = \frac{q_s}{dx}$. The formulation
340 for adverse slopes would be important in environments where they occur more commonly, but
341 initial tests indicated minimal influence in our simulations where most slopes tilt towards the
342 basin floor.

343

344 **Conditions for the Collapse of the Nonlocal, Nonlinear Model to the Linear, Local Model**

345 The nonlocal, nonlinear model (equation 11) is convenient because it collapses to the local,
346 linear model (equation 10) under certain parameter values such that the key differences between
347 the two approaches can be undone with parameter changes alone. When the slope of non-
348 deposition S_c is infinitely large, or in practice is many times greater than the greatest slopes in
349 the model domain, there is no slope-driven reduction in the deposition rate and therefore no
350 sediment bypass on steep slopes. Similarly, when the sediment transport length scale λ is equal
351 to the model grid spacing dx (this corresponds physically to a case in which sediment cannot
352 travel far over near-zero slopes), there is no transport over flat regions. Parameter values in this
353 model are therefore a direct proxy for model structure (e.g., Barnhart et al., 2020a), meaning that
354 finding parameterizations that match observations can determine optimal model structure and
355 yield insight into seascape evolution processes.

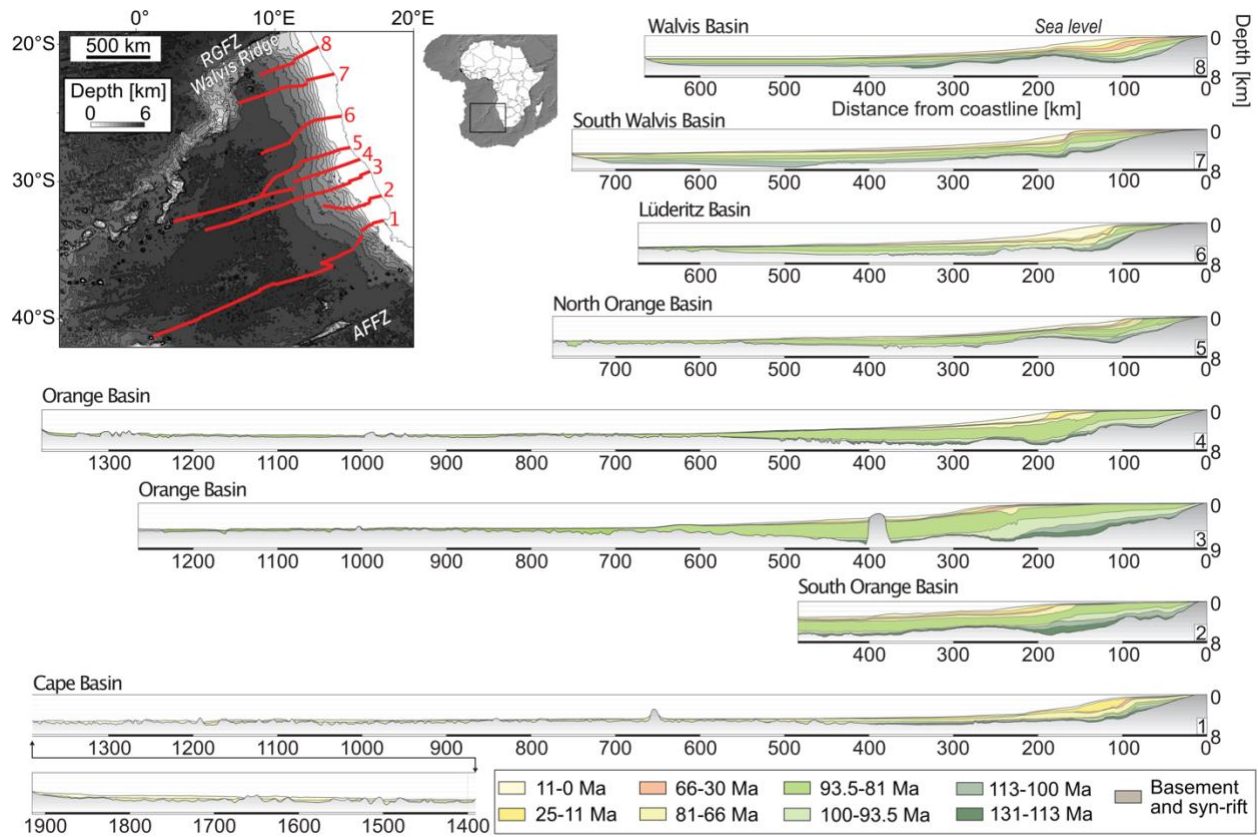
356

357 **METHOD FOR INVERSION OF PASSIVE MARGIN STRATIGRAPHY**

358 Our goal, rather than simulating margin evolution under an assumed set of parameter
359 values, is to develop insight into model structure by using a data-driven inversion to find the
360 parameter values that yield the best match between modeled and measured passive margin
361 stratigraphy. Best-fit parameter values will illuminate whether the deviations from the linear
362 diffusion approach encoded within our model (sediment bypass and long-distance transport) are
363 necessary to match observed stratigraphy.

364 **Study Area: the Southeast Atlantic Margin, Southern Africa**

365 The SAM is a well-studied passive margin sedimentary basin off the western coast of
366 southern Namibia and South Africa (Figure 2). Our study area consists of the Cape, Orange,
367 Lüderitz, and Walvis basins, which are bounded on the southeast by the Agulhas fracture zone
368 and on the northwest by the Rio Grande fracture zone. The basins were initially formed by early
369 Cretaceous rifting that opened the South Atlantic Ocean as Africa separated from South America
370 (e.g., Hirsch et al., 2010). Rifting initiated at ca. 250 Ma (Hirsch et al., 2010), but we focus only
371 on post-rift stratigraphy (Guillocheau et al., 2012; Baby et al., 2018; 2019). The earliest post-rift
372 units are dated to ca. 131 Ma (Baby et al., 2018). We selected the SAM because of the large
373 number of long (in terms of distance from the shoreline) seismic sections that have been
374 collected and interpreted (Guillocheau et al., 2012; Baby et al., 2018; 2019). Sections that have
375 continuous coverage from the shoreline to the nearly flat basin floor—typically reached at a
376 distance of between 300 and 600 km from shore on the SAM—are essential to constraining the
377 extent to which the long-distance sediment transport dynamics in our model adequately describe
378 the development of passive margin stratigraphy.



379

380 **Figure 2: Study area and seismic data, modified from Baby et al. (2019). We use sections 1 and 3-8 and retain**
 381 **the section numbers from Baby et al. (2019) for clarity. We do not use section 2 for our parameter estimation**
 382 **experiments because the thickness of deposits beyond 500 km from the shoreline is unknown. RGFZ is the**
 383 **Rio Grande Fracture Zone; AFFZ is the Agulhas-Falkland Fracture Zone.**

384

385

386 Seven seismic sections interpreted by Baby et al. (2018; 2019) comprise the dataset that
 387 we will use to test the two models and determine optimal model structure and parameter values
 388 (Figure 2). We omit one of their sections—their section 2 (Figure 2)—from our analysis because
 389 it is by far the shortest (< 500 km) and because at its end point there are deposits approximately 3
 390 km thick. It is not possible to evaluate models for long-distance sediment transport using section
 391 2 because the section ends before deposits reach a negligible thickness.

391

392

393

394

The data that is most easily compared to SFM output is the geometry of seismic reflectors. We use as our benchmark data sections that have been converted from two-way travel time to depth. Each section has nine seismic reflectors of interest, each representing the top of a particular unit as defined by Baby et al. (2019). The first (deepest) reflector of interest is the

395 contact between basement/syn-rift deposits and the first post-rift deposits, interpreted by Baby et
396 al. (2019) to occur at ca. 131 Ma. The ninth (uppermost) reflector is the modern bathymetric
397 surface. Because the basement/syn-rift surface will be manipulated as a model boundary
398 condition, there remain eight reflectors that can be used for model-data comparison when
399 determining best-fit model structure and parameter values.

400 **Inversion Methodology**

401 The procedure of our data-driven inversion approach—more formally classified as a
402 parameter inference exercise using a genetic algorithm—is to run successive “generations” (sets
403 of realizations) of the model that are run in parallel and then compared against data using a misfit
404 function we define below in the “Inversion Experimental Setup” section. The first generation
405 uses parameter values randomly drawn from a uniform distribution. Each generation yields a
406 subset of model runs with acceptable fits; a new generation of model realizations is then created
407 by randomly perturbing the parameter values (in our case using a Gaussian perturbation kernel
408 (Klinger et al., 2018)) of the runs from the previous generation that were deemed acceptable. By
409 running successive generations of realizations, the inversion procedure converges on a region of
410 the parameter space that yields best-fit parameter values. Because parameter values represent the
411 contributions of slope bypass and long-distance transport processes, best-fit parameter values
412 reveal the importance, or lack thereof, of those processes to passive margin evolution. For our
413 inversions we used the ABC-SMC (approximate Bayesian computation—sequential Monte
414 Carlo) algorithm implemented in PyABC (Klinger et al., 2018), an open-source Python package
415 that allows efficient parameter estimation using the iterative procedure described above. See
416 Sisson et al. (2007) and Toni et al. (2009) for details of ABC-SMC approaches, and Table S1 for
417 algorithm parameters used in our study.

418 There are many choices that govern inversion behavior, including the choice of the algorithm
419 itself. Our chosen approach is purposefully similar to genetic algorithm methods used in prior
420 efforts to infer parameters of SFMs (e.g., Lessenger and Cross, 1996; Bornholdt and Westphal,
421 1998; Bornholdt et al., 1999; Cross and Lessenger, 1999; Imhof and Sharma, 2006; 2007;
422 Falivene et al., 2014; Yuan et al., 2019a), but differs in the details of how successful
423 parameterizations are selected from each generation and perturbed to produce the next.
424 Exploratory testing of different parameter inference algorithm choices did not lead to
425 meaningfully different results.

426 Conducting such an inversion exercise requires estimating or assuming initial and boundary
427 conditions for the model that cannot be precisely known from geophysical and stratigraphic data
428 (for example, the subsidence history of the basin floor over the past 130 Ma). We also need to
429 define how model-data misfit will be calculated.

430 ***Model Setup and Initial and Boundary Conditions***

431 All model simulations run from 130 Ma, the approximate beginning of the post-rift
432 evolution of the SAM, to present day, with a timestep of 1,000 years. Model grid resolution is 10
433 km, a large spatial discretization but one commonly used in large-scale basin modeling (e.g.,
434 Granjeon, 2014) and that is sufficient to resolve the first-order morphology of the margin.
435 Because our goal is to invert for best-fit model parameters, rather than boundary conditions, we
436 must assume a set of boundary conditions lest we introduce too many variables into the
437 inversion. Assessment of inversion sensitivity to boundary conditions is a critical next step, but is
438 not treated here. The two key boundary conditions, both of which are functions of time, are the
439 geometry of the basement/syn-rift layer and the sediment flux to the modeled basin.

440 **Basement geometry.** The model is supplied with a value for basement elevation at every
441 point, both initially and at every subsequent timestep. We set initial basement geometry at 130
442 Ma by assuming that the initial post-rift basement had approximately 1/3 the depth, relative to a
443 steady datum, of the modern basement. We then assume that the basement subsided at an
444 exponentially declining rate (McKenzie, 1978) between 130 Ma and present, such that the
445 basement elevation over time at any point declines from its initial elevation to its known present
446 elevation, rapidly at first and then more slowly (with an e-folding time scale held constant at
447 23.67 Ma for all sections). These simplistic assumptions are broadly consistent with expectations
448 derived from simple thermal subsidence models (e.g., McKenzie, 1978) and give time series of
449 basement elevations in agreement with those deduced from basin reconstruction studies from the
450 Orange Basin (Hirsch et al., 2010). We do not model flexural subsidence due to sediment and
451 water loading (except in the sense that the deepest portions of the basement subside the fastest
452 from the initial to final condition) so that we can have consistent basement geometry between all
453 model runs for a given section to aid model comparison.

454 The other key simplification inherent to our treatment of basement geometry is that we do
455 not include any uplift or tilting of the margin over the course of its evolution. Stratigraphic
456 analysis (Rouby et al., 2009; Baby et al., 2018), thermochronologic measurements (Stanley et al.,
457 2021), basin modeling (Hirsch et al., 2010), and numerical modeling (Dauteuil et al., 2013;
458 Braun et al., 2014; Stanley et al., 2021) suggest that portions of the SAM experienced two
459 periods of rock uplift. The first was a pulse of tilting from ca. 81-66 Ma that affected the Orange
460 and Lüderitz basins and could have caused a maximum of 1,000 m of rock uplift in the proximal
461 portion of the margin (the distal portions of the margin, closer to the hinge point of the tilt, would
462 have experienced much less rock uplift; Aizawa et al., 2000; Paton et al., 2008; Hirsch et al.,

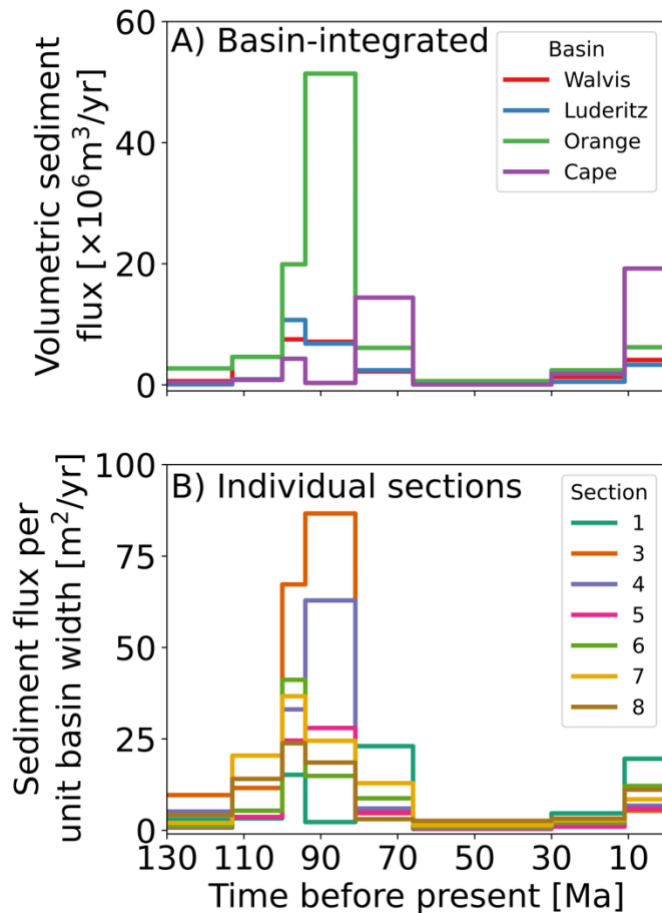
463 2010; Baby et al., 2018). This pulse is hypothesized to result from passage of Southern Africa
464 over a mantle superswell (Braun et al., 2014). The second hypothesized rock uplift pulse
465 occurred at ca. 30 Ma (though basin reconstruction studies report the pulse as occurring later at
466 ca. 16 Ma (Hirsch et al., 2010)) and had an amplitude of approximately 300-350 m (Baby et al.,
467 2018); the cause of this pulse remains unknown. We choose not to incorporate these
468 perturbations into our basement boundary condition. The magnitude and timing of uplift pulses
469 are inconsistent—and inconsistently constrained—among the four basins for which we have data
470 (Baby et al., 2018), and there is still debate about the existence and importance of the more
471 recent pulse (O'Malley et al., 2021). The magnitude of these perturbations is small relative to the
472 up to 7 km of deposits on the SAM. We acknowledge that incorporating these uplift pulses might
473 improve model-data misfit, but we argue that there is insufficient clarity in the data to
474 incorporate them, and that neglecting them would not lead to different conclusions with respect
475 to differentiating between the models we investigate.

476 ***Terrestrial sediment flux.*** The model requires a value for the terrestrial sediment flux
477 supplied to the basin at every timestep. Basin-scale sediment flux reconstructions for the SAM
478 rely on interpolation between seismic sections to derive estimates of volumetric sediment
479 delivery to the margin over the past 130 Ma (Guillocheau et al., 2012; Baby et al., 2019).
480 However, a cursory look at the sections of interest (Figure 2) shows that the total sediment
481 volume, as well as the volume during any given time interval, varies significantly among
482 sections within a given basin. To remove uncertainty surrounding the role of sediment flux, we
483 take the simplest possible approach: for each stratigraphic section to which we compare our
484 model, we calculate the sediment flux for each time period by integrating the volume of sediment
485 per unit margin width contained between each set of reflectors along each section while

486 accounting for post-deposition porosity loss due to compaction (see Shobe et al., 2022 for code).
487 This approach yields a total sediment volume per unit basin width [L^2] for each unit in each
488 section. Because the time duration represented by each section is known from previous work
489 (Guillocheau et al., 2012; Baby et al., 2018; 2019), we can then divide each unit's volume per
490 unit basin width by the time interval to get an average sediment flux to the section per unit width
491 per unit time [L^2/T]. Figure 3 shows the sediment flux time series obtained by integration, as
492 well as the basin-integrated sediment flux time series from Baby et al. (2019). The sediment flux
493 time series in any one section is reasonably similar to the basin-integrated sediment flux.
494 Estimates from our section integration approach are subject to uncertainty due to stratigraphic
495 incompleteness (e.g., Straub et al., 2020) caused by sediment moving into and out of the plane of
496 the section (i.e., parallel to the margin). There also are non-terrestrial sediments (i.e., carbonates
497 and pelagic deposits; Guillocheau et al., 2012; Baby et al., 2018) in our sections that are counted
498 as terrestrially derived sediment fluxes under our methodology. Incompleteness and non-
499 terrestrial sources likely introduce significant uncertainty into the terrestrial sediment flux
500 estimates. Given that the alternative to accepting these uncertainty sources is to assume that
501 reconstructed basin-scale sediment fluxes were evenly distributed among all sections in a given
502 basin, an idea not supported by section volumes or isopach maps (Baby et al., 2019), we argue
503 that we have made the safer assumption by conserving mass within each section we analyze to
504 enable direct comparison of modeled and measured seismic sections. Potential effects of
505 uncertainty in the sediment supply are worthy of future investigation.

506 ***Sea level.*** We hold sea level constant throughout all model experiments. The amplitude
507 of eustatic sea level variations (~120 m) is small relative to the length and depth scales of the
508 SAM both globally over the past 100 Ma (Bessin et al., 2017) and more recently throughout the

509 Quaternary off southern Africa specifically (Ramsay and Cooper, 2002). Further, the influence
510 of eustatic sea level on sediment delivery over geologic timescales to the deep, distal portions of
511 continental margins—the places where nonlocal transport dynamics may most influence
512 stratigraphy—is unclear (Sømme et al., 2009; Harris et al., 2016; 2018; 2020; Falivene et al.,
513 2020).



514

515 **Figure 3: (A) Volumetric fluxes of solid sediment from southern Africa to the four basins comprising the**
516 **SAM (Baby et al., 2019). These estimates were derived from interpolating between the sections shown in**
517 **Figure 3 (Guillocheau et al., 2012; Baby et al., 2018; 2019). (B) Volumetric solid sediment fluxes per unit**
518 **basin width derived in this study by integrating over the depth and length of each seismic section and**
519 **assuming an exponentially declining porosity profile. Given that the basins range from 500-1000 km wide, the**
520 **two estimates agree to an order of magnitude.**

521

522 *Inversion Experimental Setup*

523 We use two approaches to compare numerical model outcomes against the stratigraphic
524 record. The first (experiment 1) is to compare the modeled and measured modern bathymetric
525 surface without taking into account the geometry of subsurface reflectors. This has the advantage
526 of simplicity as it does not require accounting for the post-deposition compaction of older
527 reflectors. The second approach (experiment 2) is to simultaneously compare between the model
528 and the data the position of all reflectors (except for the top of the basement/syn-rift deposits,
529 which is a boundary condition). This latter approach is more complicated, but provides a time-
530 integrated picture of model-data (mis)fit rather than relying on only the modern surface. The
531 multi-reflector approach may be particularly important when working with data from the SAM,
532 as the geometry of the uppermost layer (11-0 Ma) is thought to be heavily influenced by contour
533 currents in addition to processes transporting sediment seaward from the coast (Baby et al.,
534 2018). In both experiments, best-fit model parameter values are constrained for each section
535 independently. This approach allows comparison of best-fit parameter values among sections to
536 assess the variability of best-fit values across the SAM.

537 For each set of experiments, we also ran an inversion using a parameterization of our model
538 that collapses to the standard linear diffusion model by setting the sediment transport length scale
539 equal to the grid spacing and removing slope as a control on the sediment deposition rate.
540 Comparison of best-fit results between the nonlocal, nonlinear model and the local, linear model
541 will reveal whether the additional complexity we have implemented to approximate nonlocal,
542 nonlinear sediment transport leads to model results that better match observations from the SAM.

543 ***Experiment 1: Calculating misfit using the modern bathymetric surface.*** In this
544 experiment we compare the modeled bathymetric surface after 130 Ma to the bathymetric
545 surface revealed in Baby et al. (2019). Because the basement elevation at 130 Ma of model time

546 is imposed to match the observed basement elevation, this is equivalent to comparing the
 547 observed (h_{obs}) and modeled (h_{sim}) thickness of sediment deposited at every point i along a
 548 section. The misfit function can be written as:

549
$$\mu = \sqrt{\frac{1}{N-1} \sum_{i=1}^{N-1} \frac{(h_{obs}-h_{sim})^2}{\delta^2}}, \quad (13)$$

550 where N is the number of cells in the model domain—and the number of points to which the
 551 seismic section has been downsampled—such that all points except for the boundary condition
 552 tied to $z = 0$ are considered. δ is the error associated with our observations. Because we do not
 553 have an explicit estimate of δ at every point, which would be a quantity derived during the
 554 seismic interpretation process, the value of δ has no influence on the inversion process because
 555 the divisor is constant throughout all of our experiments. Only in a case of spatially or
 556 temporally varying δ would its value affect the search for a best-fit set of parameter values.

557 ***Experiment 2: Calculating misfit using all reflectors.*** Our second, more sophisticated
 558 inversion scheme compares the elevation above basement of the eight reflectors from a given
 559 seismic section against the same measurements from each modeled section. This comparison
 560 gives rise to the misfit function:

561
$$\mu = \sqrt{\frac{1}{N_r(N-1)} \sum_{j=1}^{N_r} \sum_{i=1}^{N-1} \frac{(h_{obs}-h_{sim})^2}{\delta^2}}, \quad (14)$$

562 where N_r is the number of reflectors being compared between each measured and modeled
 563 section (in our case $N_r = 8$).

564 The set of possible misfit functions for an inverse problem is infinite, necessitating
 565 somewhat arbitrary choices. Our misfit functions are purely geometric—that is, they use deposit
 566 shape alone. This is appropriate given the simplicity of our model, but we note that additional
 567 constraints such as sand percentages derived from well-log data can allow the inference of

568 additional model parameters (e.g., Falivene et al., 2014). Other options for constructing misfit
569 functions include comparing deposit thickness or geometry at only a few key points (e.g., Yuan
570 et al., 2019a) or, if working in more than one planview dimension, comparing metrics of
571 planview margin geometry like the shelf edge (Zhang et al., 2021) or the stratigraphic centroid
572 (Martin et al., 2009; Granjeon, 2014).

573

574 **RESULTS AND DISCUSSION**

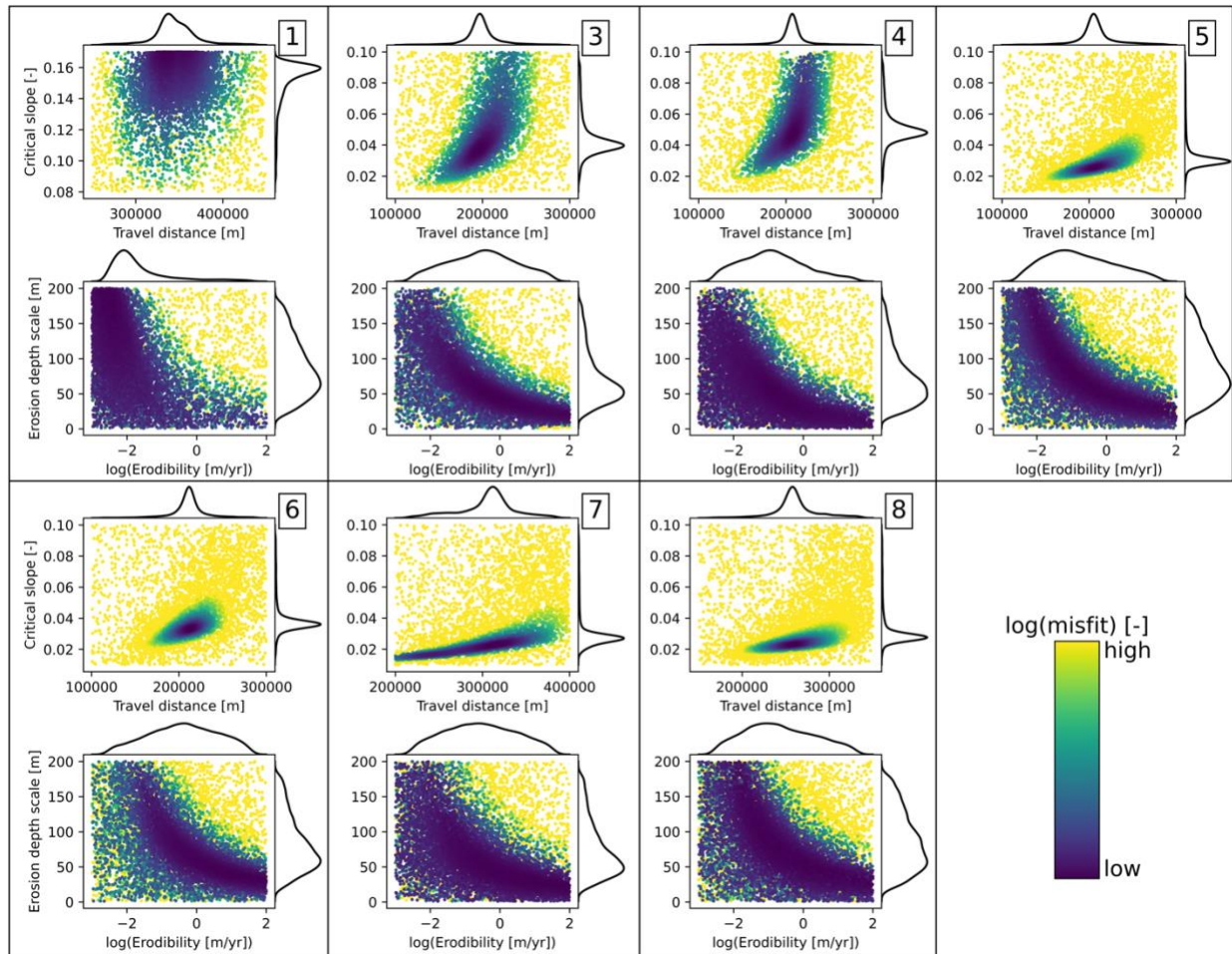
575 **The Nonlocal, Nonlinear Model Calibrated Against the Modern Bathymetric Surface**

576 *Best-fit Parameter Values*

577 Of the four parameters we varied in the nonlinear, nonlocal model, two dominate model
578 behavior and show narrow ranges that yield the best fit to the stratigraphic data (Figure 4, Table
579 S2). The two key parameters are the sediment transport distance and the slope of non-deposition.
580 Inversions converge on relatively narrow best-fit regions for these two values, such that
581 substantial deviation from the best-fit values results in much worse model-data fit. The same is
582 not true of the surface sediment erodibility and the erodibility depth scale. For all seven sections,
583 these parameters show large regions over which they provide fits of relatively unchanging
584 quality. This indicates that the sediment transport distance and slope of non-deposition drive
585 most of the variability in model outcomes. Physically, this suggests that it is the spatial pattern of
586 deposition, rather than remobilization of previously deposited sediments, that shapes the SAM.

587 Comparing parameter distributions across the seven sections (best seen in the kernel density
588 plots in Figure 4) reveals that every section converges on best-fit parameters that depart
589 significantly from the local, linear model. The majority of sections converge on values for the
590 sediment transport length scale of slightly over 2×10^5 m. Recalling that the local model is

591 recovered with a value of 10^4 m (our grid cell spacing), this result indicates that the shape of the
592 modern bathymetric surface in the SAM requires significant long-distance transport even across
593 low slopes. The best-fit slope of non-deposition is between ~ 0.02 and ~ 0.06 for all sections
594 except one—section 1—which has no portions of the parameter space that provide a good fit to
595 the data (Figure 5). Such low slopes of non-deposition imply a significant role for slope bypass,
596 or nonlocal downslope sediment transport. Best-fit S_c values many times the maximum slopes
597 observed on the SAM would indicate that sediment transport can be reasonably approximated by
598 transport that depends only on local slope (because sediment bypass becomes negligible when
599 $S \ll S_c$; equation 8, Figure 1). Given that our inverse analyses reveal S_c values ranging from
600 ~ 0.02 to ~ 0.06 in the sections where we find reasonable model-data fit, we do not find support
601 for the local transport approximation. Instead, the best fit between modeled and measured
602 stratigraphy is achieved when sediment can bypass slopes of more than a few degrees.



603

604 **Figure 4: Results for all seven sections from the search for a best-fit parameterization of the nonlocal,**
 605 **nonlinear model with the inversion procedure constrained only by the modern bathymetric surface. Scatter**
 606 **plots show model-data misfit (color) as a function of the four key parameters. Kernel density estimate (KDE)**
 607 **plots show the distribution of values for each parameter. Because the inversion procedure runs more model**
 608 **realizations in regions of the parameter space with reduced model-data misfit, peaks in the KDE plots can be**
 609 **interpreted as showing the region of each parameter's range that leads to the lowest misfit. Narrow peaks in**
 610 **the KDE plots indicate parameters with well-constrained best-fit values, while broad peaks indicate**
 611 **parameters for which a wide range of values produces similar misfit. Numbered sets of plots refer to the**
 612 **seismic section used for the inversion. Maximum and minimum misfit values vary between sections; color**
 613 **values have been scaled for interpretability.**

614

615 *Comparison of Modeled and Observed Stratigraphy*

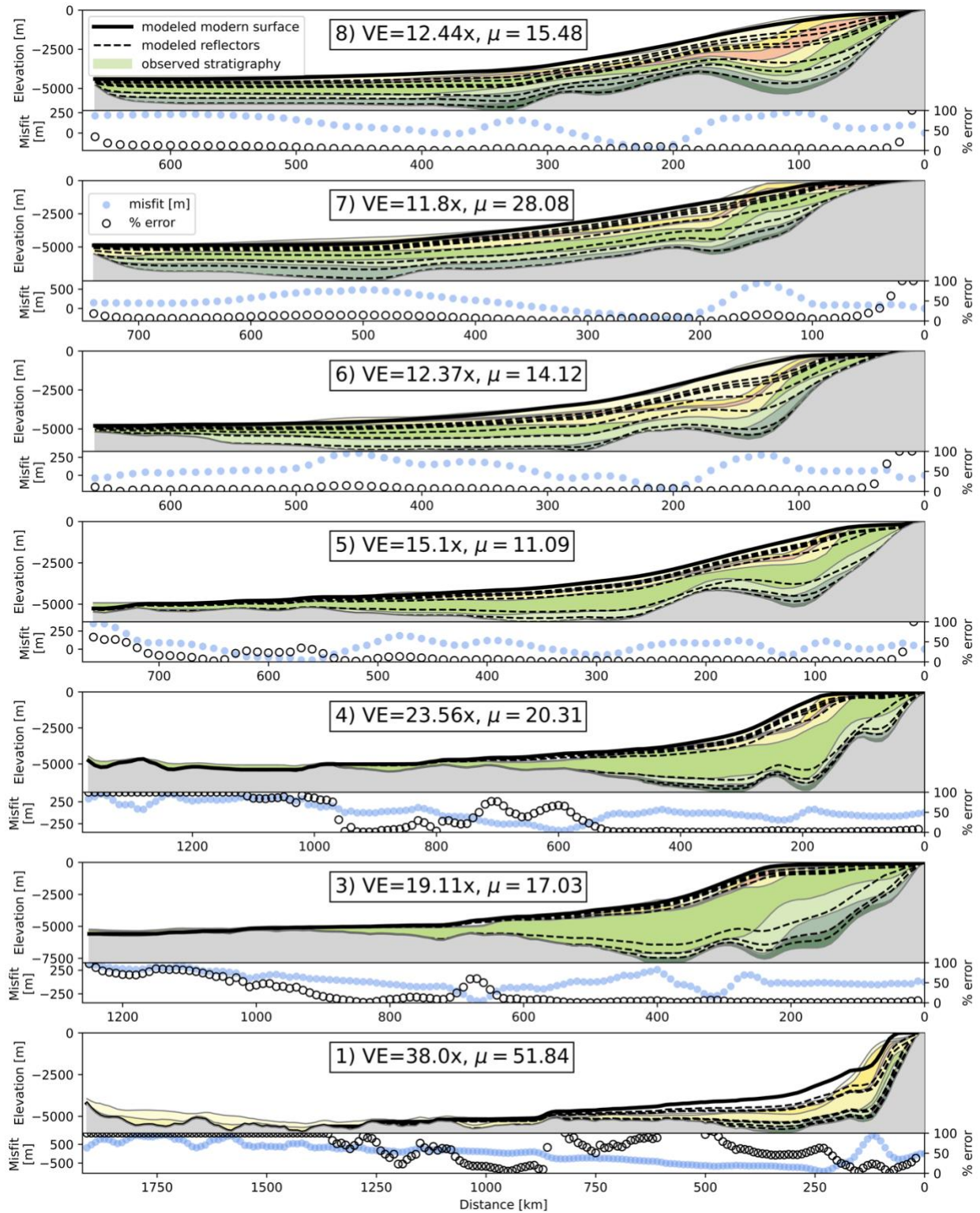
616 For five of the seven sections, the inversion yielded best-fit parameter estimates that led to
 617 best-fit simulations that qualitatively and quantitatively fit the data reasonably well (Figure 5).

618 These sections have gently sloping continental shelves with altitudes below, rather than level
 619 with, sea level, and smooth, convex-up shelf edges. They have concave-up continental slopes

620 grading into gently sloping continental rise/abyssal plain deposits. Sediment is not always found
621 as far from shore as in the data, but noticeable accumulations of sediment are observed up to
622 ~1000 km from shore. Two sections, 1 and 7, yielded what we interpret to be substantially worse
623 fits as defined by the mismatch of major morphometric features like the continental shelf edge
624 and the curvature of the continental slope. It is difficult to know why the fits are substantially
625 worse for sections 1 and 7. One key commonality that the two sections share is a relatively high
626 proportion of the total sediment volume stored at the extreme distal end of the section. While our
627 approach does allow for more realistic modeling of long-runout sediment transport than the
628 classic local, linear approach does, there is still a fundamental tension in which allowing
629 sediment to accumulate at the very distal end of the modeled section requires too much inhibition
630 of deposition at the proximal end. It may not be possible for our model to deposit enough
631 sediment in distal reaches while preserving steep, well-defined shelf edges. This weakness would
632 not be resolved in section 1 by raising the maximum possible S_c value (Figure 4); increases in S_c
633 would further inhibit transport to the basin floor.

634 Comparison of modeled and observed subsurface reflectors, though it was not quantitatively
635 incorporated into the misfit function in this experiment, shows that the pattern of reflectors is
636 almost completely depositional. There are few—and only minor—instances of reflectors being
637 truncated by overlying units, indicating that the story in these models is one of continuous
638 deposition rather than episodes of deposition and re-erosion driven by variations in the terrestrial
639 sediment flux time series. This is broadly concordant with the interpreted geologic history of the
640 SAM, in which—barring the episodes of rock uplift that we have not modeled here—there is
641 little erosional truncation of units except by eustatic variations in the nearshore. This
642 concordance of modeled and observed stratigraphy suggests that our model is not only producing

643 reasonable final bathymetry, but is building a stratigraphic record that reflects the long-term
644 average of the processes shaping the SAM.



645
646
647
648
649

Figure 5: Comparison between modeled and measured stratigraphy for all seven sections with two measures of misfit. While all modeled reflectors are shown (and are compacted to account for overburden), only the modern bathymetric surface was used to assess model-data fit in this experiment; subsurface modeled reflectors were not compared against data to assess fit. Percent error points that appear to be missing are

650 >100%; Values of exactly 100% error typically occur where the model deposited no sediment. μ is total misfit
651 given by equation 13; VE is vertical exaggeration.
652

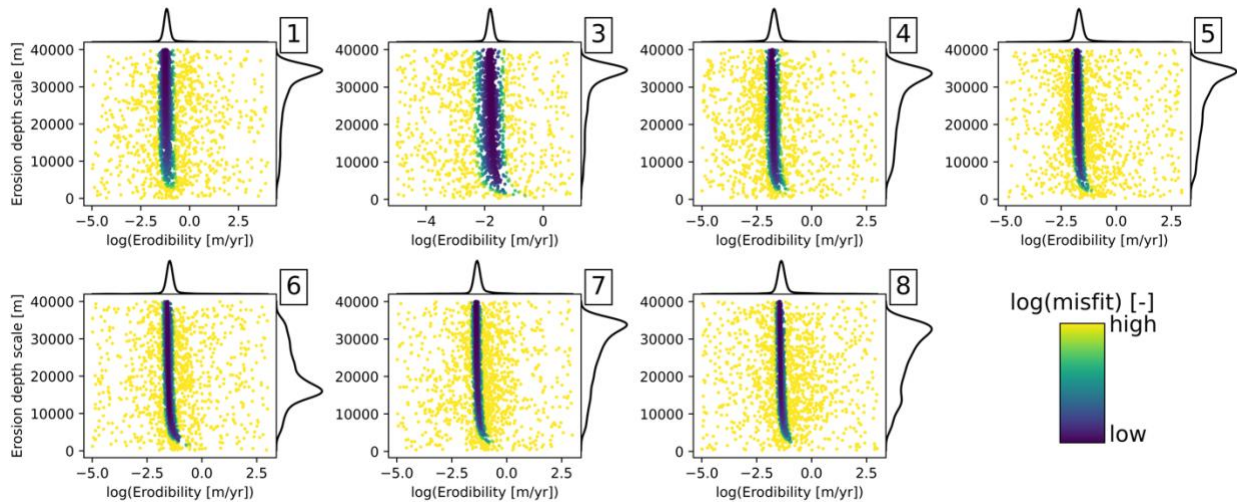
653 **Comparison Between the Nonlocal, Nonlinear Model and the Local, Linear Model**

654 Here we compare inversion results between the two models to assess whether the nonlocal,
655 nonlinear model leads to substantially better fits between modeled and measured stratigraphy.
656 We search for the best-fit local, linear model using the same procedure as for our new model; the
657 only two parameters to optimize in the local, linear model are the surface sediment erodibility K_e
658 and the depth scale over which it decays d_* .

659 Using only the modern bathymetric surface as a constraint, the local, linear model converges
660 to a narrow range of surface erodibility values and a broader region of erodibility decay depths
661 for sections 3-8 (Figure 6, Table S2). Section 1, ever the outlier, converges on a large erodibility
662 value that decays rapidly with depth. All sections except section 6 indicate that the model is
663 “searching” for erodibility decay depth values even greater than the 40,000 m maximum value in
664 the inversion. At the maximum values of 40,000 m, erodibility in the deepest parts of the margin
665 only declines to ~80% of its value at the water surface such that sediment entrainment can still
666 occur in the deep, distal reaches of the margin wherever nonzero slopes are found. We interpret
667 this behavior as the local, linear model compensating for its lack of mechanisms for long-
668 distance sediment transport by allowing substantial erosion at great depth. Interestingly, the
669 tendency of the inversion procedure to identify d_* values large enough that sediment erodibility
670 does not meaningfully decline with depth suggests that while erodibility decay with depth may
671 give rise to realistic-looking shallow marine morphometric features like shelf breaks (Kaufman
672 et al., 1992; van Balen et al., 1995), such an approach may ultimately be counterproductive when
673 we expand our view to include the distal portion of the margin because it yields models that

674 cannot transport sediment far enough from shore without some other process or additional
 675 changes in erodibility with depth or distance from shore.

676



677

678 **Figure 6: Results for all seven sections from the search for best-fit parameter values for the local, linear**
 679 **diffusion model constrained only by the modern bathymetric surface. The tall, narrow region of good-fitting**
 680 **models indicates that only a narrow range of surface erodibility values leads to minimized misfit. The**
 681 **majority of sections (all except 6) have converged to the maximum values of the erodibility decay depth scale,**
 682 **indicating that even higher values would lead to further improvements in model-data fit. Given that under**
 683 **our imposed maximum value of 40,000 m, erodibility in the deepest regions of the margin only declines to**
 684 **~80% of its value at the water surface, further improvements to model-data fit from increasing the maximum**
 685 **decay depth would be marginal.**

686

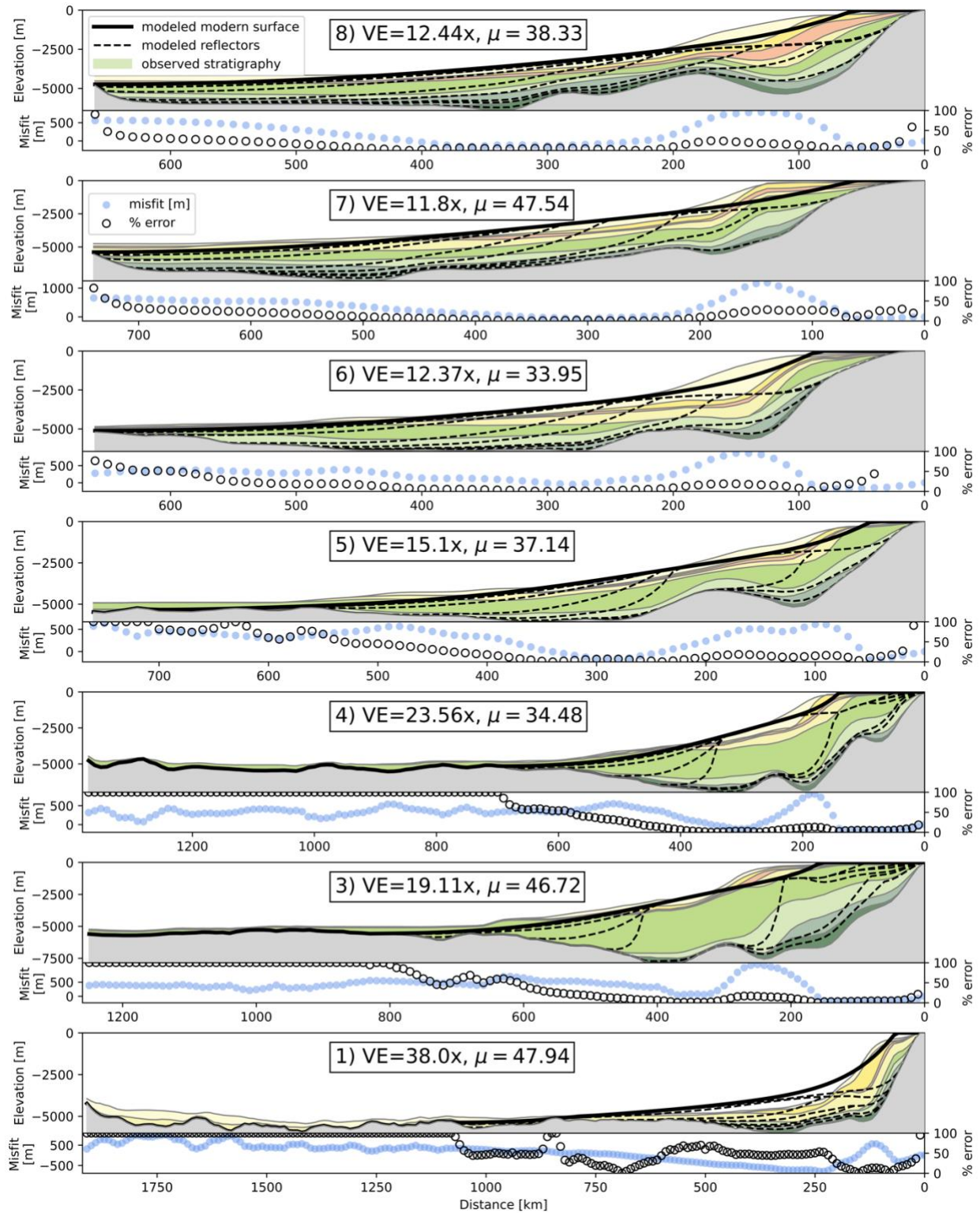
687 The local, linear model provides, for all sections that can be reasonably fit by either
 688 approach, a worse fit to the modern bathymetric surface than was obtained with the nonlocal,
 689 nonlinear model (Figure 7, 8). While best-fit parameterizations of the local, linear model do
 690 exhibit sediment delivery to the distal portions of the sections (achieved through large erodibility
 691 decay depths that yield non-negligible erodibility at depth), this comes at the cost of model-data
 692 fit in the nearshore environment. The large erodibility decay depths required to enable transport
 693 of sediment far from shore precludes the local, linear model from achieving the rounded, shallow
 694 continental shelf edge observed in the data. Instead, a shelf of sorts is created simply by
 695 progradation of the shoreline as sediments accumulate in the nearshore but are prevented from

696 accumulating above sea level under the assumption that the shoreline will prograde under such
697 conditions. Shoreline progradation, combined with an erodibility that is nearly constant
698 throughout the depth profile, results in sharp shelf breaks grading immediately into the concave-
699 up continental slope rather than the smooth, convex-up shelf breaks observed in the seismic data.
700 The local, linear model is effectively being forced to choose between accurately reproducing the
701 shelf edge and delivering sediment to the distal portions of the margin. Because our misfit
702 function incorporates every point along each section, the model minimizes misfit if it delivers
703 sediment far from shore even at the cost of reproducing the shelf and shelf-edge. A misfit
704 function that focused on the nearshore (e.g., Yuan et al., 2019a) would likely lead to the opposite
705 end-member of this tradeoff.

706 Though our misfit function in this experiment did not incorporate comparison between
707 observed and modeled subsurface reflectors, the local, linear model—even in its best-fit
708 parameterizations—does not stand up to a qualitative assessment of the form of the subsurface
709 reflectors it produces (Figure 7). To deliver sediment far from shore, the local, linear model must
710 first deposit that sediment in a proximal location and then erode those deposits during times of
711 low terrestrial sediment flux. The time series of reflectors produced in most of the local, linear
712 best-fit simulations reveal a steep, prograding wedge of sediment that is then smoothed out to
713 lower gradients through subsequent erosion. Except for the brief periods in SAM history when
714 the margin experienced substantial rock uplift, which we do not model, there is limited evidence
715 for significant erosional truncation beyond that occurring in the nearshore due to eustatic
716 variations (Baby et al., 2018). The reflectors from the nonlocal, nonlinear model (Figure 5) do
717 not show this pattern of progradation of a steep-fronted sediment wedge followed by later
718 truncation by erosion; they instead show consistent accumulation of sediments through time at

719 any given location, including the distal reaches of the basin. Interpretation of the stratigraphic
720 record suggests that the latter behavior is more consistent with the history of the SAM.

721 It is unsurprising that the nonlocal, nonlinear model provides a better fit to the data than the
722 local, linear model (Figure 8) in all but one case where neither model provided a reasonable fit
723 and imposed parameter ranges prevented the more complex model from fully minimizing misfit
724 (Figure 4)—the latter model is a restricted subset of the former. The critical results of this
725 comparison are that (1) the model requires significant deviation from linear diffusion parameter
726 values (i.e., a large travel distance relative to the model grid cell spacing and a critical slope low
727 enough that sediment bypass is common) to provide a reasonable match between modeled and
728 observed bathymetry, (2) the local, linear model cannot through parameter adjustments provide
729 fits that approximate the outcomes of the nonlocal, nonlinear model, (3) the dynamics of the
730 local, linear model as revealed by subsurface reflectors are not supported by observations from
731 the SAM, and (4) seven of eight sections show a reduction in misfit—and four of seven sections
732 show at least a factor of two reduction—achieved by adding nonlocal, nonlinear transport
733 dynamics (Figure 8). This suggests that long-distance transport and slope-dependent sediment
734 bypass processes are required to form the canonical shapes of passive margin stratigraphy, and
735 therefore argues that these processes are essential ingredients in SFMs, at least for passive
736 margin settings.



737

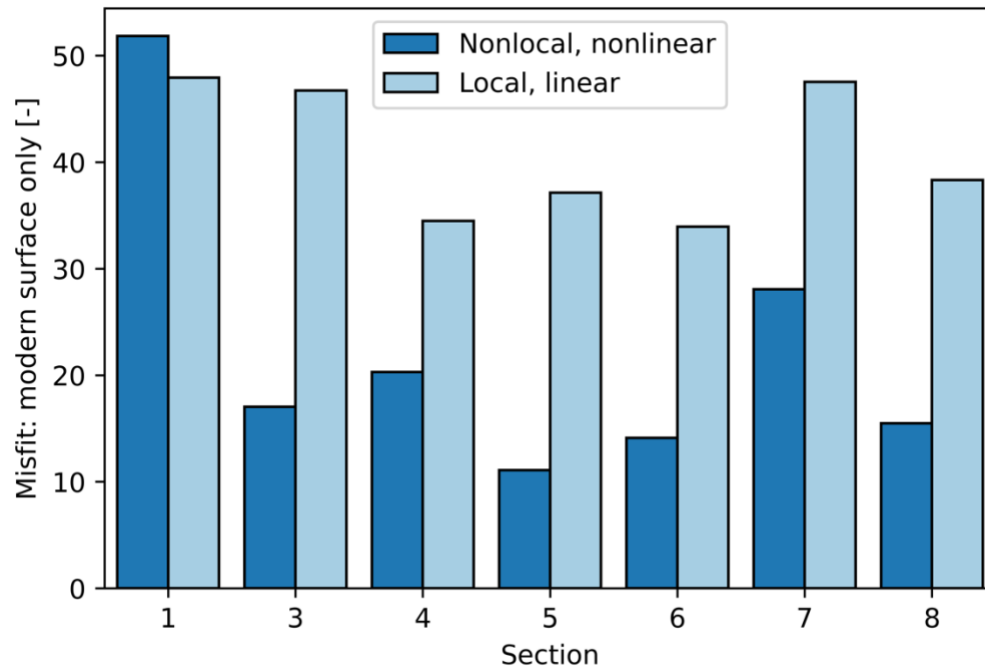
738

739

740

Figure 7: Comparison between modeled and measured stratigraphy for the best-fit local, linear diffusion model realization for each section. Bottom panels show two measures of misfit. While all modeled reflectors are shown (and are compacted to account for overburden), only the modern bathymetric surface was used to

741 assess model-data fit in this experiment; subsurface modeled reflectors were not compared against data to
742 assess fit. μ is total misfit given by equation 13; VE is vertical exaggeration.
743



744 **Figure 8: Misfit values for the best-fit model for each section using the nonlocal, nonlinear model (dark blue)**
745 **and the local, linear model (light blue) when the model fit is determined by comparing only against the**
746 **modern bathymetric surface. The nonlocal, nonlinear model yields better fitting best-fit realizations for six of**
747 **seven sections.**
748
749

750 **The Influence of Considering Multiple Reflectors**

751 Parameters estimated by the inversion that takes into account all eight reflectors are surprisingly
752 similar to those estimated when using only the modern bathymetric surface to constrain the
753 inversion. For brevity we show average parameter values for the 50 best-fitting model
754 realizations from the single reflector and multiple-reflector inversions plotted against each other
755 (Figure 9) such that points falling on the 1:1 line indicate consistent parameter values achieved
756 by the two methods. See Table S3 and Figures S1-S4 for detailed results of multi-reflector
757 inversions.

758 Inclusion of all reflectors in the misfit calculation for the nonlocal, nonlinear model
759 resulted in a shift towards slightly greater best-fit travel distance values (Figure 9A), likely

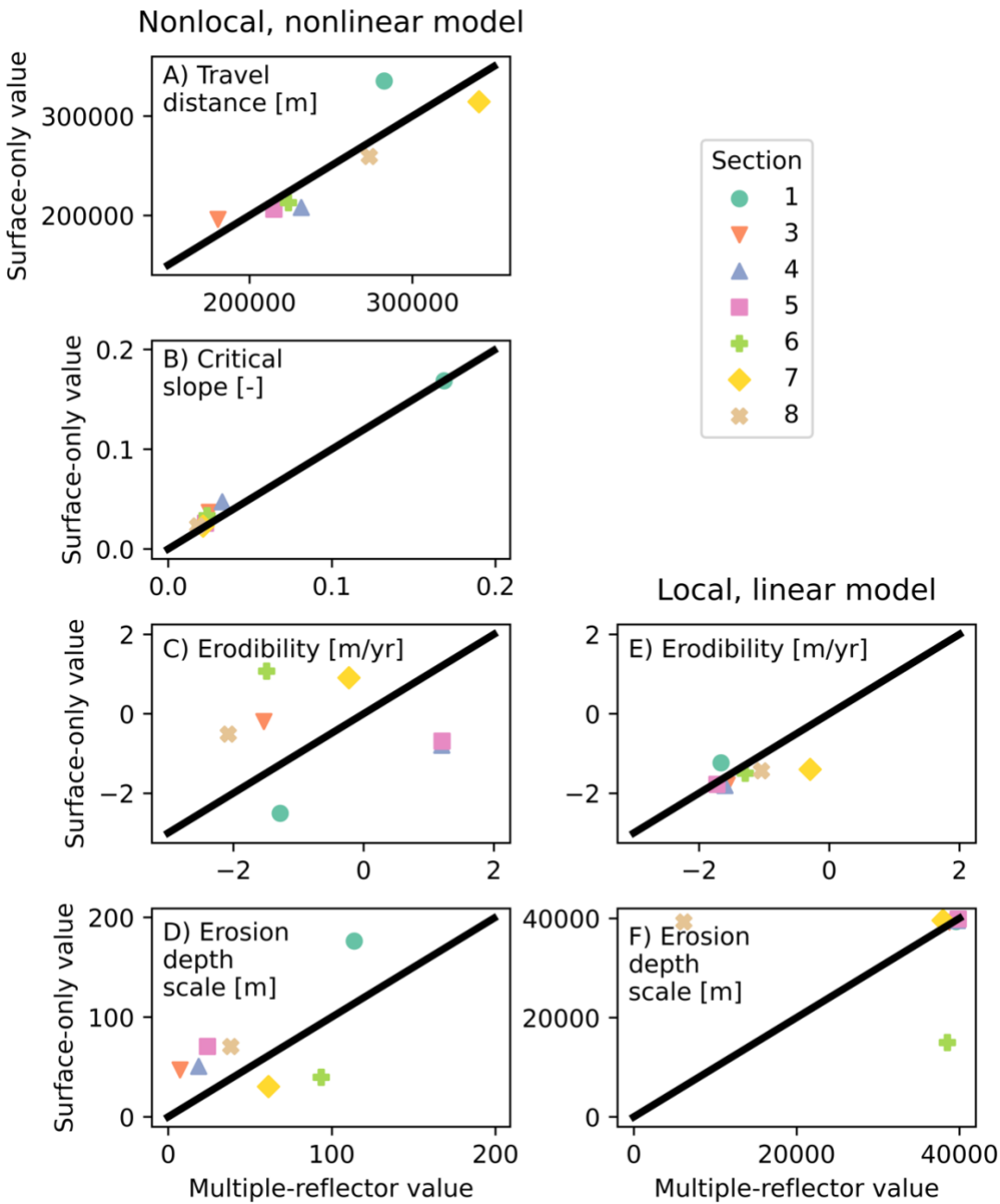
760 because the data requires that good-fitting models be able to distribute sediment to the distal
761 portion of the basin even relatively early in the margin's evolution when there do not yet exist
762 the slopes required to drive sediment bypass in the absence of another mechanism for long-
763 distance transport. The critical slope of non-deposition (Figure 9B) remained remarkably
764 consistent between the surface-only and multiple-reflector inversions, suggesting that the model
765 most effectively adjusts to the need to deliver early deposits far from shore with changes in the
766 travel distance, which affects transport over all slopes, rather than the critical slope, which only
767 affects transport over meaningful gradients. Physically this may indicate the importance of long-
768 runout sediment transport processes (e.g., turbidity currents, marine debris flows) that may
769 initially be generated by significant bathymetric slopes but then transport sediment up to
770 hundreds of km over vanishingly low slopes. The erodibility and erosion depth scale (Figure 9C
771 and D, respectively) show more scatter between inversion methods; this is not surprising given
772 that there is a large region of good-fitting values for both parameters (e.g., Figure 4).

773 Including all reflectors when searching for best-fit parameters for the local, linear model
774 leads to surface erodibility values that largely fall near the 1:1 line (Figure 9E), indicating that
775 the composition of the misfit function did not have a strong effect on the best-fit value. The same
776 is true of the erodibility decay depth scale (Figure 9F) with the exception of two values that
777 changed significantly between the surface-only and multiple-reflector inversion schemes. We
778 attribute the overall consistency between parameter values derived using the two different
779 methods to the fact that all reflectors in our seismic data show a similar pattern: long-distance
780 transport beginning from the earliest stages of post-rift margin evolution followed by the largely
781 depositional draping of successive units atop previous deposits. In this respect the modern
782 surface is not geometrically distinct from the subsurface reflectors, which may explain why

783 incorporating the subsurface reflectors leads to little improvement in model-data fit. A model can
784 either achieve parameter values that allow it to develop these types of deposits (i.e., in the
785 nonlocal, nonlinear model) in which case the specific number and age of reflectors used does not
786 have a significant effect on inferred best-fit parameter values, or it cannot achieve
787 parameterizations that allow long-distance, deposition-driven stratal stacking patterns (i.e., in the
788 local, linear model) in which case the specifics of the misfit function do not matter because the
789 fit to eight reflectors will be no better than the fit to a single one. We initially undertook the
790 multiple-reflector inversion because the modern bathymetric surface is thought to be heavily
791 influenced by contour currents (Baby et al., 2018). Adding seven subsurface reflectors does not
792 substantially change inferred best-fit parameters, which may indicate that variability in contour
793 current effects among units does not cause a radical enough change in stratigraphic
794 architecture—relative to the effects of subsidence and terrestrial sediment flux—to influence our
795 simple models.

796 When the misfit function incorporates all eight reflectors, the nonlocal, nonlinear model
797 yields a better fit to the observed stratigraphic data than the local, linear model does for all seven
798 sections (Figure 10). The improvement in model-data fit gained from adding nonlocal, nonlinear
799 sediment transport dynamics exists regardless of whether we use only the modern surface or all
800 reflectors as a basis for comparison. The misfit values between the two models are much closer
801 when all reflectors are used for the inversion (Figure 10). This arises from the introduction of
802 seven additional constraints on the model, many of which it must inevitably fail to match (Figure
803 5) even in its best-fit parameterization. However, the consistent reduction in misfit that
804 accompanies the nonlocal, nonlinear model signals that those dynamics are required to produce
805 stratigraphy that matches observations. The only scenario where this would not hold true is one

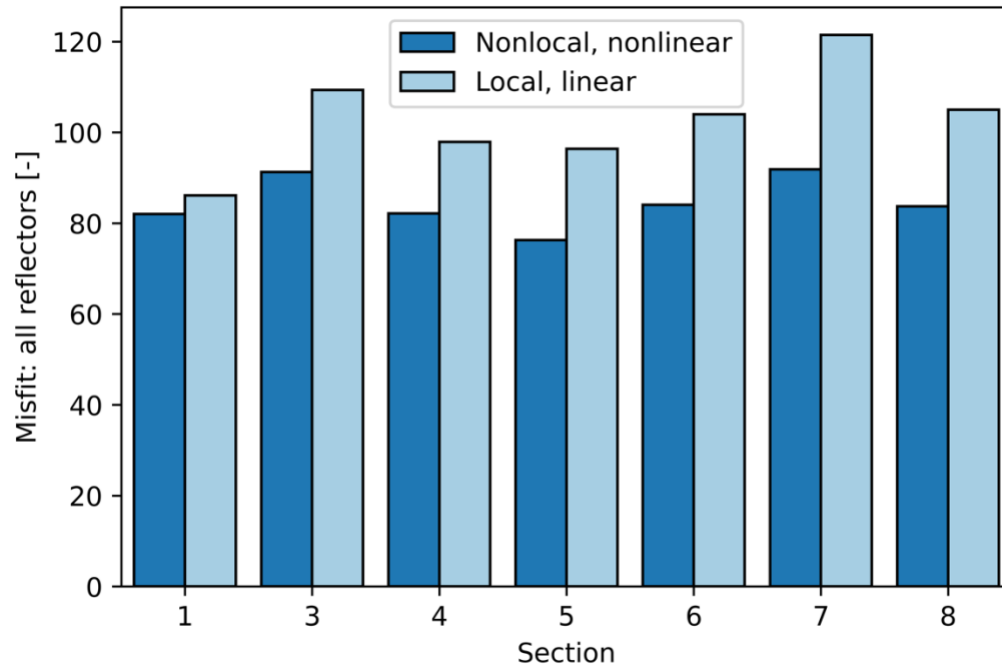
806 in which a misfit function was used that did not take into account the distal portions of the basin
 807 at all. Given the substantial accumulations of sediment in the distal portions of the SAM (Figure
 808 2), we argue that finding models that adequately simulate those deposits is a prerequisite for
 809 closing the source-to-sink mass balance.



810

811 **Figure 9: Comparison between best-fit parameter values derived from the surface-only inversion and the**
 812 **multiple-reflector inversion. Black lines indicate a 1:1 match between parameter values derived by the two**

813 **methods. In the case of the nonlinear, nonlocal model (column 1), the two most important parameters fall**
 814 **close to the 1:1 line, indicating that the inversion method (whether subsurface information is incorporated or**
 815 **not) does not have a strong influence on the best-fit parameter values and therefore on predicted margin**
 816 **stratigraphy. In the case of the local, linear model (column 2), erodibility values are consistent between**
 817 **methods while erosion depth scale values show more scatter.**
 818



819 **Figure 10: Misfit values for the best-fit model for each section using the nonlocal, nonlinear model (dark blue)**
 820 **and the local, linear model (light blue) when the model fit is determined by comparing against all seismic**
 821 **reflectors. The nonlocal, nonlinear model yields better fitting best-fit realizations for all seven sections.**
 822
 823

824 **Limitations and Implications for Inversion of the Stratigraphic Record**

825 Our motivation in testing SFMs is to enable the inversion of the stratigraphic record for
 826 information about past terrestrial environments and geomorphic processes. If reasonably
 827 effective SFM structures and parameterizations can be identified *a priori*, then coupled
 828 LEM/SFMs will be more useful for inferring drivers of past landscape evolution. Our results
 829 favor the idea that SFMs should incorporate mechanisms for sediment bypass and long-distance
 830 transport, and that these processes cannot be adequately mimicked with parameter changes in the
 831 commonly used local, linear diffusion model for seascape evolution. Our study further
 832 emphasizes that *both* mechanisms of nonlocality (bypass and long-distance transport) are

833 required to achieve the model-data agreement we find; Figure 4 demonstrates that one element or
834 the other is not sufficient to place the model in the good-fitting region of the parameter space.

835 The nonlocal, nonlinear model we tested represents an amalgamation of ideas from
836 previous workers that have not previously been evaluated in detail against stratigraphic data, and
837 our analysis reveals that it provides a substantial improvement over the more widely used local,
838 linear model. However, the nonlocal, nonlinear model still needs improvement. Aside from
839 subsuming a wide array of marine transport processes into two key transport parameters, its most
840 critical shortcoming is that it only heuristically accounts for the momentum that allows transport
841 processes like turbidity currents and marine debris flows to carry sediment into the distal
842 portions of basins. More effective conceptualizations of sediment entrainment and
843 disentrainment, possibly following recent advances in hillslope geomorphology (e.g., Doane et
844 al., 2018; Furbish et al., 2021), might further improve SFMs with the understanding that the
845 models will always need to simulate the spatial and temporal average of marine sediment
846 transport if they are to prove feasible for inverse analyses that require 10^5 - 10^6 forward model
847 realizations. Improving model fit—especially abrupt slope breaks driven by changes in process
848 dominance—may require multiprocess models (e.g., Granjeon et al., 1999; Syvitski and Hutton,
849 2001), but their parameter-rich nature may hinder parameter estimation exercises and make them
850 susceptible to overfitting to a given calibration location. There exist sufficient models in the
851 literature that span a wide range of complexity that, as in this study, the future challenge is more
852 about rigorously testing models against data to find the simplest workable theory than it is about
853 developing new models.

854 Though we used seven seismic sections spanning four basins to evaluate different SFMs,
855 our study is limited to a single passive margin. Best-fit regions of the parameter space for the

856 nonlinear, nonlocal model's travel distance and critical slope of non-deposition parameters
857 consistently showed that the model was not collapsing to its local, linear parameterization, but
858 the key parameters still exhibited considerable variability among sections (Figure 4). While our
859 analysis may have restricted the range of possible values that need to be considered when using
860 such a model to invert the stratigraphic record, a set of global parameter values cannot be
861 assumed. Similarly, we have not established sensitivity of inversion outcomes to initial and
862 boundary conditions and additional processes—including eustatic sea level, lithospheric flexure,
863 and terrestrial sediment supply—which are well-understood in the SAM relative to other regions
864 but still carry considerable uncertainty (e.g., Guillocheau et al., 2012).

865 Flexure is a process of particular interest given that it can influence the location of
866 depocenters and resulting stratal geometries. We have not treated flexure here to ensure that
867 modeled stratigraphy is compared in the context of a consistent time-evolving basement
868 geometry. We suspect that adding flexure to the model would not alter the conclusion that
869 nonlocal processes govern the development of passive margin stratigraphy. The generally
870 proximal deposition in the local, linear model (Figure 7) might cause flexural subsidence in those
871 locations, thereby potentially reducing bathymetric slopes and resulting fluxes of sediment
872 towards the distal portions of the basin. The longer-distance deposition given by the nonlocal,
873 nonlinear model (Figure 5) may result in less proximal flexural subsidence and the maintenance
874 of greater bathymetric slopes, allowing enhanced transport towards the deep, distal portions of
875 the margin. Nonetheless, the relative importance of nonlocal transport processes in models
876 including flexural subsidence is important to examine.

877 A final open question is the applicability of our findings given the reduced
878 dimensionality of our modeling exercise. We tested 2-D implementations of our candidate

879 models. This means that the models enforced purely margin-perpendicular sediment transport,
880 when in reality margin-parallel components of transport—such as contour currents that are
881 known to have influenced the SAM (Baby et al., 2018)—also occur. Our 2-D implementations
882 also cannot simulate processes that cause the development of preferential sediment transport
883 pathways, like submarine canyons and channels. We therefore must interpret the improvement in
884 fit given by our nonlocal, nonlinear model as arising due to the model’s ability to simulate
885 average sediment transport patterns that occur as a result of nonlocal processes whose effects
886 likely vary spatially over geologic time, like for example a submarine channel undergoing
887 avulsions across a deep-sea fan. Though there exist plenty of 3-D SFMs (e.g., Granjeon and
888 Joseph, 1999; Salles et al., 2018; Falivene et al., 2019), testing optimal SFM structure in two
889 dimensions remains an important stepping stone towards inverting terrestrial landscape history
890 from stratigraphy because the simplicity and parsimony of 2-D models allows relatively efficient
891 calibration even in data-poor situations.

892

893 **CONCLUSIONS**

894 We evaluated a simple, nonlocal, nonlinear model for marine sediment transport and the
895 development of marine stratigraphy over geologic time. The model builds on the concepts of
896 sediment bypass espoused by previous authors (e.g., Syvitski et al., 1998; Ross et al., 1994; Ding
897 et al., 2019a;) that have not previously been directly tested against observed stratigraphy.
898 Quantitative comparison of the model against seven stratigraphic sections from the SAM reveals
899 that:

- 900 1. The nonlocal, nonlinear model can achieve parameterizations that develop realistic
901 marine bathymetry and stratigraphy, though variability in best-fit parameter values exists
902 among the seven seismic sections tested.
- 903 2. The nonlocal, nonlinear model does not converge on parameter values that result in a
904 collapse to the local, linear model. The local, linear model cannot fit the data. It fails both
905 to fit the modern bathymetric surface and to yield seascape evolution trajectories that
906 match observations.
- 907 3. The key difference between the two models lies in the ability of the nonlocal, nonlinear
908 model to deliver sediment to distal portions of the basin without compromising its ability
909 to develop realistic nearshore morphology and stratigraphy.
- 910 4. Points (1) through (3) hold true regardless of whether model parameters are optimized
911 using only the modern bathymetric surface or the full suite of subsurface seismic
912 reflectors, indicating that our results are robust to the specifics of the misfit function
913 employed.
- 914 5. Processes of sediment bypass and long-distance transport govern the architecture of the
915 stratigraphic record over basin-filling timescales, making it essential that SFMs capture at
916 least the spatial and temporal averages of these nonlocal processes.

917

918 Given the general lack of terrestrial evidence for past landscape evolution dynamics, the
919 stratigraphic record represents our best chance to learn about the erosion trajectories of
920 landscapes long gone. We tentatively suggest that the transport dynamics encapsulated in the
921 nonlocal, nonlinear model govern the development of passive margin stratigraphy. Our ability to
922 invert the stratigraphic record, either on its own for inferring sediment supply to basins or

923 coupled with landscape evolution models to infer past tectonic, climatic, and/or lithologic
924 boundary conditions, would benefit from improved understanding of such nonlocal transport
925 processes.

926
927 **ACKNOWLEDGMENTS**

928 Model code, data, and inversion scripts are publicly available at
929 <https://doi.org/10.6084/m9.figshare.20205077> (Shobe et al., 2022). C.M. Shobe was supported
930 by H2020 Marie Skłodowska-Curie Actions grant no. 833132 (STRATASCAPE). We
931 acknowledge time on the West Virginia University Thorny Flat high-performance computing
932 cluster which is supported by the National Science Foundation under Major Research
933 Instrumentation program award #1726534. We thank Benoît Bovy, Tim Carr, Rachel Glade, Kim
934 Huppert, Luca Malatesta, Delphine Rouby, Jaime Toro, and Amy Weislogel for helpful
935 discussions. Thanks to Guillermo Franco, Nate Garver-Daniels, and Daniel Turpen for HPC
936 support and to Xuesong Ding, Oriol Falivene, and Associate Editor Peter Burgess for
937 constructive reviews.

938 **REFERENCES CITED**

939 Aizawa, M., Bluck, B., Cartwright, J., Milner, S., Swart, R., and Ward, J., 2000, Constraints on
940 the geomorphological evolution of Namibia from the offshore stratigraphic record,
941 Communications of the Geological Survey of Namibia, v. 12, p. 337—346.
942 Allen, P.A. and Allen, J.R., 2013, Basin Analysis, Principles and Application to Petroleum Play
943 Assessment, Wiley-Blackwell, 632 p.
944 Andrews, D.J. and Bucknam, R.C., 1987, Fitting degradation of shoreline scarps by a nonlinear
945 diffusion model, Journal of Geophysical Research: Solid Earth, v. 92, no. B12, p. 12857—
946 12867, doi:10.1029/JB092iB12p12857.

- 947 Baby, G., Guillocheau, F., Morin, J., Ressouche, J., Robin, C., Broucke, O., and Dall'Asta, M.,
948 2018, Post-rift stratigraphic evolution of the Atlantic margin of Namibia and South Africa:
949 Implications for the vertical movements of the margin and the uplift history of the South
950 African Plateau, *Marine and Petroleum Geology*, v. 97, p. 169—191,
951 doi:10.1016/j.marpetgeo.2018.06.030.
- 952 Baby, G., Guillocheau, F., Braun, J., Robin, C., and Dall'Asta, M., 2019, Solid sedimentation
953 rates history of the Southern African continental margins: Implications for the uplift
954 history of the South African Plateau, *Terra Nova*, v. 32, no. 1, p. 53—65,
955 doi:10.1111/ter.12435.
- 956 van Balen, R.T., van der Beek, P.A., and Cloetingh, S.A.P.L., 1995, The effect of rift shoulder
957 erosion on stratal patterns at passive margins: Implications for sequence stratigraphy, *Earth
958 and Planetary Science Letters*, v. 134, p. 527—544, doi:10.1016/0012-821X(95)98955-L.
- 959 Barnhart, K.R., Glade, R.C., Shobe, C.M., and Tucker, G.E., 2019, Terrainbento 1.0: a Python
960 package for multi-model analysis in long-term drainage basin evolution, *Geoscientific
961 Model Development*, v. 12, p. 1267—1297, doi:10.5194/gmd-12-1267-2019.
- 962 Barnhart, K.R., Tucker, G.E., Doty, S., Shobe, C.M., Glade, R.C., Rossi, M.W., and Hill, M.C.,
963 2020a, Inverting topography for landscape evolution model process representation: Part 1,
964 conceptualization and sensitivity analysis, *Journal of Geophysical Research: Earth Surface*,
965 v. 125, no. 7, doi:10.1029/2018JF004961.
- 966 Barnhart, K.R., Tucker, G.E., Doty, S., Shobe, C.M., Glade, R.C., Rossi, M.W., and Hill, M.C.,
967 2020b, Inverting topography for landscape evolution model process representation: Part 2,
968 calibration and validation, *Journal of Geophysical Research: Earth Surface*, v. 125, no. 7,
969 doi:10.1029/2018JF004963.

- 970 Barnhart, K.R., Tucker, G.E., Doty, S., Shobe, C.M., Glade, R.C., Rossi, M.W., and Hill, M.C.,
971 2020c, Inverting topography for landscape evolution model process representation: Part 3,
972 determining parameter ranges for select mature geomorphic transport laws and connecting
973 changes in fluvial erodibility to changes in climate, *Journal of Geophysical Research: Earth*
974 *Surface*, v. 125, no. 7, doi:10.1029/2019JF005287.
- 975 Beaumont, C., Fullsack, P., and Hamilton, J., 1992, Erosional control of active compressional
976 orogens, *in* McClay, K.R., ed., *Thrust tectonics*, p. 1—18.
- 977 van der Beek, P., and Bishop, P., 2003, Cenozoic river profile development in the Upper Lachlan
978 catchment (SE Australia) as a test of quantitative fluvial incision models, *Journal of*
979 *Geophysical Research: Solid Earth*, v. 108, no. B6, doi:10.1029/2002JB002125.
- 980 Bessin, P., Guillocheau, F., Robin, C., Braun, J., Bauer, H., and Schroëtter, J.-M., 2017,
981 Quantification of vertical movement of low elevation topography combining a new
982 compilation of global sea-level curves and scattered marine deposits (Armorican Massif,
983 western France), *Earth and Planetary Science Letters*, v. 470, p. 25—36,
984 doi:10.1016/j.epsl.2017.04.018.
- 985 Bornholdt, S., and Westphal, H., 1998, Automation of stratigraphic simulations: quasi-backward
986 modeling using genetic algorithms, *in*: Mascle, A., Puigdefabregas, C., Luterbacher, H.P.,
987 and Fernandez, M., eds., *Cenozoic Foreland Basins of Western Europe*, Geological Society
988 *Special Publications* v. 134, p. 371-379.
- 989 Bornholdt, S., Nordlund, U., and Westphal, H., 1999, Inverse stratigraphic modeling using
990 genetic algorithms, *in*: Harbaugh, J.W., Watney, W.L., Rankey, E.C., Slingerland, R.,
991 Goldstein, R.H., and Franseen, E.K., eds., *Numerical Experiments in Stratigraphy: Recent*

- 992 Advances in Stratigraphic and Sedimentologic Computer Simulations,
993 doi:10.2110/pec.99.62.0085.
- 994 Braun, J., 2021, Comparing the transport-limited and ζ -q models for sediment transport, *Earth*
995 *Surface Dynamics*, v. 10, p. 301-327, doi:10.5194/esurf-10-301-2022.
- 996 Braun, J., Deschamps, F., Rouby, D., and Dauteuil, O., 2013, Flexure of the lithosphere and the
997 geodynamical evolution of non-cylindrical rifted passive margins: Results from a
998 numerical model incorporating variable elastic thickness, surface processes and 3D thermal
999 subsidence, *Tectonophysics*, v. 604, p. 72—82, doi:10.1016/j.tecto.2012.09.033.
- 1000 Braun, J., Guillocheau, F., Robin, C., Baby, G., and Jelsma, H., 2014, Rapid erosion of the
1001 Southern African Plateau as it climbs over a mantle superswell, *Journal of Geophysical*
1002 *Research: Solid Earth*, v. 119, p. 6093—6112, doi:10.1002/2014JB010998.
- 1003 Burgess, P.M., Lammers, H., van Oosterhout, C., and Granjeon, D., 2006, Multivariate sequence
1004 stratigraphy: Tackling complexity and uncertainty with stratigraphic forward modeling,
1005 multiple scenarios, and conditional frequency maps, *American Association of Petroleum*
1006 *Geologists Bulletin*, v. 90, no. 12, p. 1883—1901, doi:10.1306/06260605081.
- 1007 Burgess, P.M., 2012, A brief review of developments in stratigraphic forward modelling 2000-
1008 2009, *in* Roberts, D.G. and Bally, A.W., eds., *Regional Geology and Tectonics: Principles*
1009 *of Geologic Analysis*, p. 378-404.
- 1010 Campforts, B., Shobe, C.M., Steer, P., Vanmaercke, M., Lague, D., and Braun, J., 2020,
1011 HyLands 1.0: a Hybrid Landscape evolution model to simulate the impact of landslides
1012 and landslide-derived sediment on landscape evolution, v. 13., p. 3863—3886,
1013 doi:10.5194/gmd-13-3863-2020.

- 1014 Carretier, S., Martinod, P., Reich, M., and Godderis, Y., 2016, Modelling sediment clasts
1015 transport during landscape evolution, *Earth Surface Dynamics*, v. 4, p. 237—251,
1016 doi:10.5194/esurf-4-237-2016.
- 1017 Cross, T.A. and Lessenger, M.A., 1999, Construction and application of a stratigraphic inverse
1018 model, *in*: Harbaugh, J.W., Watney, W.L., Rankey, E.C., Slingerland, R., Goldstein, R.H.,
1019 and Franseen, E.K., eds., *Numerical Experiments in Stratigraphy: Recent Advances in*
1020 *Stratigraphic and Sedimentologic Computer Simulations*, doi:10.2110/pec.99.62.0069.
- 1021 Dauteuil, O., Rouby, D., Braun, J., Guillocheau, F., and Deschamps, F., 2013, Post-breakup
1022 evolution of the Namibian margin: Constrains from numerical modeling, *Tectonophysics*,
1023 v. 604, p. 122—138, doi:10.1016/j.tecto.2013.03.034.
- 1024 Davy, P. and Lague, D., 2009, Fluvial erosion/transport equation of landscape evolution models
1025 revisited, *Journal of Geophysical Research*, v. 114, F03007, doi:10.1029/2008JF001146.
- 1026 DiBiase, R.A. and Whipple, K.X., 2011, The influence of erosion thresholds and runoff
1027 variability on the relationships among topography, climate, and erosion rate, *Journal of*
1028 *Geophysical Research*, v. 116, doi:10.1029/2011JF002095.
- 1029 Ding, X., Salles, T., Flament, N., Mallard, C., and Rey, P.F., 2019a, Drainage and sedimentary
1030 responses to dynamic topography, *Geophysical Research Letters*, v. 46, no. 24, p. 14385—
1031 14394, doi:10.1029/2019GL084400.
- 1032 Ding, X., Salles, T., Flament, N., and Rey, P., 2019b, Quantitative stratigraphic analysis in a
1033 source-to-sink numerical framework, *Geoscientific Model Development*, v. 12, p. 2571—
1034 2585, doi:10.5194/gmd-12-2571-2019.
- 1035 Doane, T.H., Furbish, D.J., Roering, J.J., Schumer, R., and Morgan, D.J., 2018, Nonlocal
1036 sediment transport on steep lateral moraines, Eastern Sierra Nevada, California, USA,

- 1037 Journal of Geophysical Research: Earth Surface, v. 123, no. 1, p. 187—208,
1038 doi:10.1002/2017JF004325.
- 1039 Falivene, O., Frascati, A., Gesbert, S., Pickens, J., Hsu, Y., and Rovira, A., 2014, Automatic
1040 calibration of stratigraphic forward models for predicting reservoir presence in exploration,
1041 American Association of Petroleum Geologists Bulletin, v. 98, no. 9, p. 1811-1835,
1042 doi:10.1306/02271413028.
- 1043 Falivene, O., Frascati, A., Bolla Pittaluga, M., and Martin, J., 2019, Three-dimensional reduced-
1044 complexity simulation of fluvio-deltaic clastic stratigraphy, Journal of Sedimentary
1045 Research, v. 89, p. 46-65, doi:10.2110/jsr.2018.73.
- 1046 Falivene, O., Prather, B.E., and Martin, J., 2020, Quantifying sand delivery to deep water during
1047 changing sea-level: Numerical models from the Quaternary Brazos Icehouse continental
1048 margin, Basin Research, v. 32, p. 1711-1733, doi:10.1111/bre.12449.
- 1049 Foufoula-Georgiou, E., Ganti, V., and Dietrich, W.E., 2010, A nonlocal theory of sediment
1050 transport on hillslopes, Journal of Geophysical Research: Earth Surface, v. 115, no. F2,
1051 doi:10.1029/2009JF001280.
- 1052 Furbish, D.J. and Roering, J.J., 2013, Sediment disentrainment and the concept of local versus
1053 nonlocal transport on hillslopes, Journal of Geophysical Research: Earth Surface, v. 118,
1054 no. 2, p. 937—952, doi:10.1002/jgrf.20071.
- 1055 Furbish, D.J., Roering, J.J., Doane, T.H., Roth, D.L., Williams, S.G., and Abbott, A.M., 2021,
1056 Rarefied particle motions on hillslopes—Part 1: Theory, Earth Surface Dynamics, v. 9, np.
1057 3, p. 539—576, doi:10.5194/esurf-9-539-2021.
- 1058 Granjeon, D. and Joseph, P., 1999, Concepts and applications of a 3-D multiple lithology,
1059 diffusive model in stratigraphic modeling, *in*: Harbaugh, J.W., Watney, W.L., Rankey,

- 1060 E.C., Slingerland, R., Goldstein, R.H., and Franseen, E.K., eds., Numerical Experiments in
1061 Stratigraphy: Recent Advances in Stratigraphic and Sedimentologic Computer Simulations,
1062 p. 197—210, doi:10.2110/pec.99.62.0197.
- 1063 Granjeon, D., 2014, 3D forward modelling of the impact of sediment transport and base level
1064 cycles on continental margins and incised valleys, International Association of
1065 Sedimentology Special Publication, v. 46, p. 453-472.
- 1066 Guerit, L., Yuan, X.P., Carretier, S., Bonnet, S., Rohais, S., Braun, J., and Rouby, D., 2019,
1067 Fluvial landscape evolution controlled by the sediment deposition coefficient: Estimation
1068 from experimental and natural landscapes, *Geology*, v. 47, no. 9, p. 853—856,
1069 doi:10.1130/G46356.1.
- 1070 Guillocheau, F., Rouby, D., Robin, C., Helm, C., Rolland, N., Le Carlier de Veslud, C., and
1071 Braun, J., 2012, Quantification and causes of the terrigenous sediment budget at the scale
1072 of a continental margin: a new method applied to the Namibia-South Africa margin, *Basin
1073 Research*, v. 24, p. 3—30, doi:10.1111/j.1365-2117.2011.00511.x.
- 1074 Harris, A.D., Covault, J.A., Madof, A.S., Sun, T., Sylvester, Z., and Granjeon, D., 2016, Three-
1075 dimensional numerical modeling of eustatic control on continental-margin sand
1076 distribution, *Journal of Sedimentary Research*, v. 86, p. 1434-1443,
1077 doi:10.2110/jsr.2016.85.
- 1078 Harris, A.D., Baumgartner, S.E., Sun, T., and Granjeon, D., 2018, A poor relationship between
1079 sea level and deep-water sand delivery, *Sedimentary Geology*, v. 370, p. 42-51,
1080 doi:10.1016/j.sedgeo.2018.04.002.
- 1081 Harris, A.D., Covault, J.A., Baumgartner, S., Sun, T., and Granjeon, D., 2020, Numerical
1082 modeling of icehouse and greenhouse sea-level changes on a continental margin: Sea-level

- 1083 modulation of deltaic avulsion processes, *Marine and Petroleum Geology*, v. 111, p. 807-
1084 814, doi:10.1016/j.marpetgeo.2019.08.055.
- 1085 Hereema, C.J. et al., 2020, What determines the downstream evolution of turbidity currents?
1086 *Earth and Planetary Science Letters*, v. 532, doi:10.1016/j.epsl.2019.116023.
- 1087 Hirsch, K.K., Schenck-Wenderoth, M., van Wees, J.-D., Kuhlmann, G., and Paton, D.A., 2010,
1088 Tectonic subsidence history and thermal evolution of the Orange Basin, *Marine and*
1089 *Petroleum Geology*, v. 27, p. 565—584, doi:10.1016/j.marpetgeo.2009.06.009.
- 1090 Hopley, D.E.J., Sinclair, H.D., Mudd, S.M., and Cowie, P.A., 2011, Field calibration of sediment
1091 flux dependent river incision, *Journal of Geophysical Research: Earth Surface*, v. 116, no.
1092 F4, doi:10.1029/2010JF001935.
- 1093 Imhof, M.G. and Sharma, A.K., 2006, Quantitative seismostratigraphic inversion of a prograding
1094 delta from seismic data, *Marine and Petroleum Geology*, v. 23, p. 735-744,
1095 doi:10.1016/j.marpetgeo.2006.04.004.
- 1096 Imhof, M.G. and Sharma, A.K., 2007, Seismostratigraphic inversion: Appraisal, ambiguity, and
1097 uncertainty, *Geophysics*, v. 72, no. 4, p. R51-R66, doi:10.1190/1.2720496.
- 1098 Jerolmack, D.J. and Paola, C., 2010, Shredding of environmental signals by sediment transport,
1099 *Geophysical Research Letters*, v. 37, no. 19, doi:10.1029/2010GL044638.
- 1100 Kaufman, P., Grotzinger, J.P., and McCormick, D.S., 1992, Depth-dependent diffusion algorithm
1101 for simulation of sedimentation in shallow marine depositional systems, *Kansas Geological*
1102 *Survey Bulletin*, v. 233, p. 489—508.
- 1103 Kenyon, P.M. and Turcotte, D.L., 1985, Morphology of a delta prograding by bulk sediment
1104 transport, *Geological Society of America Bulletin*, v. 96, no. 11, p. 1457—1465,
1105 doi:10.1130/0016-7606(1985)96<1457:MOADPB>2.0.CO;2.

- 1106 Klinger, E., Rickert, D., and Hasenauer, J., 2018, pyABC: distributed, likelihood-free inference,
1107 *Bioinformatics*, v. 34, no. 20, p. 3591—3593, doi:10.1093/bioinformatics/bty361.
- 1108 Kooi, H. and Beaumont, C., 1994, Escarpment evolution on high-elevation rifted margins:
1109 Insights derived from a surface processes model that combines diffusion, advection, and
1110 reaction, *Journal of Geophysical Research*, v. 99, no. 12, p. 12191—12209.
- 1111 Lessenger, M.A. and Cross, T.A., 1996, An inverse stratigraphic simulation model—is
1112 stratigraphic inversion possible? *Energy Exploration and Exploitation*, v. 14, no. 6, p.
1113 627—637, doi:10.1177/014459879601400606.
- 1114 Lowe, D.R., Grain flow and grain flow deposits, *Journal of Sedimentary Petrology*, v. 46, no. 1,
1115 p. 188—199.
- 1116 Luchi, R., Balachandar, S., Seminara, G., and Parker, G., 2018, Turbidity currents with
1117 equilibrium basal driving layers: A mechanism for long runout, *Geophysical Research*
1118 *Letters*, v. 45, no. 3, p. 1518—1526, doi:10.1002/2017GL075608.
- 1119 Martin, J., Paola, C., Abreu, V., Neal, J., and Sheets, B., 2009, Sequence stratigraphy of
1120 experimental strata under known conditions of differential subsidence and variable base
1121 level, *American Association of Petroleum Geologists Bulletin*, v. 93, no. 4, p. 503-533,
1122 doi:10.1306/12110808057.
- 1123 McKenzie, D., 1978, Some remarks on the development of sedimentary basins, *Earth and*
1124 *Planetary Science Letters*, v. 40, no. 1, p. 25—32, doi:10.1016/0012-821X(78)90071-7.
- 1125 Mohrig, D., Ellis, C., Parker, G., Whipple, K.X., and Hondzo, M., 1998, Hydroplaning of
1126 subaqueous debris flows, *Geological Society of America Bulletin*, v. 110, no. 3, p. 387—
1127 394, doi:10.1130/0016-7606(1998)110<0387:HOSDF>2.3.CO;2.

- 1128 Molnar, P., Brown, E.T., Burchfiel, B.C., Deng, Q., Feng, X., Li, J., Raisbeck, G.M., Shi, J.,
1129 Zhangming, W., Yiou, F., and You, H., 1994, Quaternary climate change and the
1130 formation of river terraces across growing anticlines on the north flank of the Tien Shan,
1131 China, *The Journal of Geology*, v. 102, no. 5, p. 583—602, doi:10.1086/629700.
- 1132 Moretti, I. and Turcotte, D.L., 1985, A model for erosion, sedimentation, and flexure with
1133 application to New Caledonia, *Journal of Geodynamics*, v. 3, no. 1—2, p. 155—168,
1134 doi:10.1016/0264-3707(85)90026-2.
- 1135 O'Malley, C.P.B., White, N.J., Stephenson, S.N., and Roberts, G.G., 2021, Large-scale tectonic
1136 forcing of the African Landscape, *Journal of Geophysical Research: Earth Surface*, v.
1137 126, doi:10.1029/2021JF006345.
- 1138 Niedoroda, A.W., Reed, C.W., Swift, D.J.P., Arato, H., and Hoyanagi, K., 1995, Modeling
1139 shore-normal large-scale coastal evolution, *Marine Geology*, v. 126, p. 181—199,
1140 doi:10.1016/0025-3227(95)98961-7.
- 1141 Paola, C., 2000, Quantitative models of sedimentary basin filling, *Sedimentology*, v. 47, no. s1,
1142 p. 121—178, doi:10.1046/j.1365-3091.2000.00006.x.
- 1143 Parker, G., Fukushima, Y., and Pantin, H.M., 1986, Self-accelerating turbidity currents, *Journal*
1144 *of Fluid Mechanics*, v. 171, p. 145—181, doi:10.1017/S0022112086001404.
- 1145 Paton, D.A., van der Spuy, D., di Primio, R., and Horsfield, B., 2008, Tectonically induced
1146 adjustment of passive-margin accommodation space: influence on the hydrocarbon
1147 potential of the Orange Basin, South Africa, *American Association of Petroleum*
1148 *Geologists Bulletin*, v. 92, no. 5, p. 589—609, doi:10.1306/12280707023.

- 1149 Pazzaglia, F.J. and Brandon, M.T., 1996, Macrogeomorphic evolution of the post-Triassic
1150 Appalachian mountains determined by deconvolution of the offshore basin sedimentary
1151 record, *Basin Research*, v. 8, no. 3, p. 255—278, doi:10.1046/j.1365-2117.1996.00274.x.
- 1152 Pirmez, C., Pratson, L.F., and Steckler, M.S., 1998, Clinoform development by advection-
1153 diffusion of suspended sediment: Modeling and comparison to natural systems, *Journal of*
1154 *Geophysical Research*, v. 103, no. B10, p. 24141—24157, doi:10.1029/98JB01516.
- 1155 Poag, C.W., 1992, U.S. Middle Atlantic continental rise: Provenance, dispersal, and deposition
1156 of Jurassic to Quaternary sediments, *in* Poag, C.W. and Graciansky, P.C., eds., *Geologic*
1157 *Evolution of Atlantic Continental Rises*: Springer, p. 100—156.
- 1158 Poag, C.W. and Sevon, W.D., 1989, A record of Appalachian denudation in postrift Mesozoic
1159 and Cenozoic sedimentary deposits of the U.S. Middle Atlantic continental margin,
1160 *Geomorphology*, v. 2, no. 1—3, p. 119—157, doi:10.1016/0169-555X(89)90009-3.
- 1161 Ramsay, P.J. and Cooper, J.A.G., 2002, Late Quaternary sea-level change in South Africa,
1162 *Quaternary Research*, v. 57, no. 1, p. 82—90, doi:10.1006/qres.2001.2290.
- 1163 Rivenaes, J.C., 1992, Application of a dual-lithology, depth-dependent diffusion equation in
1164 stratigraphic simulation, *Basin Research*, v. 4, p. 133—146, doi:10.1111/j.1365-
1165 2117.1992.tb00136.x.
- 1166 Rivenaes, J.C., 1997, Impact of sediment transport efficiency on large-scale sequence
1167 architecture: results from stratigraphic computer simulation, *Basin Research*, v. 9, p. 91—
1168 105, doi:10.1046/j.1365-2117.1997.00037.x.
- 1169 Roering, J.J., Kirchner, J.W., and Dietrich, W.E., 1999, Evidence for nonlinear, diffusive
1170 sediment transport on hillslopes and implications for landscape morphology, *Water*
1171 *Resources Research*, v. 35, no. 3, p. 853—870, doi:10.1029/1998WR900090.

- 1172 Ross, W.C., Halliwell, B.A., May, J.A., Watts, D.E., and Syvitski, J.P.M., 1994, Slope
1173 readjustment: A new model for the development of submarine fans and aprons, *Geology*,
1174 v. 22, p. 511—514, doi:10.1130/0091-7613(1994)022<0511:SRANMF>2.3.CO;2.
- 1175 Rouby, D., Bonnet, S., Guillocheau, F., Gallagher, K., Robin, C., Biancotto, F., Dauteuil, O., and
1176 Braun, J., 2009, Sediment supply to the Orange sedimentary system over the last 150 My:
1177 An evaluation from sedimentation/denudation balance, *Marine and Petroleum Geology*,
1178 v. 26, no. 6, p. 782-794, doi:10.1016/j.marpetgeo.2008.08.004.
- 1179 Rouby, D., Braun, J., Robin, C., Dauteuil, O., and Deschamps, F., 2013, Long-term stratigraphic
1180 evolution of Atlantic-type passive margins: A numerical approach of interactions
1181 between surface processes, flexural isostasy and 3D thermal subsidence, *Tectonophysics*,
1182 v. 604, p. 83—103, doi:10.1016/j.tecto.2013.02.003.
- 1183 Sadler, P.M., 1981, Sediment accumulation rates and the completeness of stratigraphic sections,
1184 *The Journal of Geology*, v. 89, no. 5, p. 569—584, doi:10.1086/628622.
- 1185 Salles, T., 2019, eSCAPE: Regional to global scale landscape evolution model v2.0,
1186 *Geoscientific Model Development*, v. 12, p. 4165—4184, doi:10.5194/gmd-12-4165-
1187 2019.
- 1188 Salles, T. and Hardiman, L., 2016, Badlands: An open-source, flexible and parallel framework to
1189 study landscape dynamics, *Computers & Geosciences*, v. 91, p. 77—89,
1190 doi:10.1016/j.cageo.2016.03.011.
- 1191 Salles, T., Ding, X., and Brocard, G., 2018, pyBadlands: A framework to simulate sediment
1192 transport, landscape dynamics and basin stratigraphic evolution through space and time,
1193 *PLoS ONE*, v. 13, no. 4, doi:10.1371/journal.pone.0195557.

- 1194 Schanz, S.A., Montgomery, D.R., Collins, B.D., and Duvall, A.R., 2018, Multiple paths to
1195 straths: A review and reassessment of terrace genesis, *Geomorphology*, v. 312, p. 12—
1196 23, doi:10.1016/j.geomorph.2018.03.028.
- 1197 Sclater, J.G. and Christie, P.A.F., 1980, Continental Stretching: An explanation of the Post-Mid-
1198 Cretaceous subsidence of the central North Sea Basin, *Journal of Geophysical Research:*
1199 *Solid Earth*, v. 85, no. B7, p. 3711—3739, doi:10.1029/JB085iB07p03711.
- 1200 Shobe, C.M., Tucker, G.E., and Barnhart, K.R., 2017, The SPACE 1.0 model: a Landlab
1201 component for 2-D calculation of sediment transport, bedrock erosion, and landscape
1202 evolution, *Geoscientific Model Development*, v. 10, no. 12, p. 4577—4604,
1203 doi:10.5194/gmd-10-4577-2017.
- 1204 Shobe, C.M., Braun, J., Yuan, X.P., Campforts, B., Gailleton, B., Baby, G., Guillocheau, F., and
1205 Robin, C., 2022, Code and data to accompany "Inverting passive margin stratigraphy for
1206 marine sediment transport dynamics over geologic time": Figshare data set, (available at
1207 <https://doi.org/10.6084/m9.figshare.20205077>).
- 1208 Sisson, S.A., Fan, Y., and Tanaka, M.M. (2007) Sequential Monte Carlo without likelihoods,
1209 *Proceedings of the National Academy of Sciences*, v. 104, no. 6, p. 1760-1765,
1210 doi:10.1073/pnas.0607208104.
- 1211 Sømme, T.O., Helland-Hansen, W., and Granjeon, D., 2009, Impact of eustatic amplitude
1212 variations on shelf morphology, sediment dispersal, and sequence stratigraphic
1213 interpretation: Icehouse versus greenhouse systems, *Geology*, v. 37, no. 7, p. 587-590,
1214 doi:10.1130/G25511A.1.
- 1215 Steckler, M.S., Reynolds, D.J., Coakley, B.J., Swift, B.A., and Jarrad, R., 1993, Modelling
1216 passive margin sequence stratigraphy, *in*: Posamentier, H.W., Summerhayes, C.P., Haq,

- 1217 B.U., and Allen, G.P., eds., *Sequence Stratigraphy and Facies Associations*, p. 19—41,
1218 doi:10.1002/9781444304015.ch2.
- 1219 Steckler, M.S., Swift, D.J.P., Syvitski, J.P., Goff, J.A., and Niedoroda, A.W., 1996, Modeling the
1220 sedimentology and stratigraphy of continental margins, *Oceanography*, v. 9, no. 3, p.
1221 183—188.
- 1222 Steckler, M.S., Watts, A.B., and Thorne, J.A., 1988, Subsidence and basin modeling at the U.S.
1223 Atlantic passive margin, *in*: Sheridan, R.E. and Grow, J.A., eds., *The Atlantic Continental*
1224 *Margin, U.S.: Geological Society of America, The Geology of North America*, v. 1—2, p.
1225 399—416..
- 1226 Stanley, J.R., Braun, J., Baby, G., Guillocheau, F., Robin, C., Flowers, R.M., Brown, R.,
1227 Wildman, M., and Beucher, R., Constraining plateau uplift in southern Africa by
1228 combining thermochronology, sediment flux, topography, and landscape evolution
1229 modeling, *Journal of Geophysical Research: Solid Earth*, v. 126, no. 7,
1230 doi:10.1029/2020JB021243.
- 1231 Straub, K.M., Duller, R.A., Foreman, B.Z., and Hajek, E.A., 2020, Buffered, incomplete, and
1232 shredded: The challenges of reading an imperfect stratigraphic record, *Journal of*
1233 *Geophysical Research: Earth Surface*, v. 125, no. 3, doi:10.1029/2019JF005079.
- 1234 Syvitski, J.P.M., Smith, J.N., Calabrese, E.A., and Boudreau, B.P., 1988, Basin sedimentation
1235 and the growth of prograding deltas, *Journal of Geophysical Research: Oceans*, v. 93, no.
1236 C6, p. 6895—6906, doi:10.1029/JC093iC06p06895.
- 1237 Syvitski, J.P.M. and Hutton, E.W.H., 2001, 2D SEDFLUX 1.0C:: an advance process-response
1238 numerical model for the fill of marine sedimentary basins, *Computers & Geosciences*, v.
1239 27, no. 6, p. 731—753, doi:10.1016/S0098-3004(00)00139-4.

- 1240 Talling, P.J., Summer, E.J., Masson, D.G., and Malgesini, G., 2012, Subaqueous sediment
1241 density flows: Depositional processes and deposit types, *Sedimentology*, v. 59, p. 1937—
1242 2003, doi:10.1111/j.1365-3091.2012.01353.x.
- 1243 Thran, A.C., East, M., Webster, J.M., Salles, T., and Petit, C., 2020, The influence of carbonate
1244 platforms on the geomorphological development of a mixed carbonate-siliciclastic margin
1245 (Great Barrier Reef, Australia), *Geochemistry, Geophysics, Geosystems*, v. 21,
1246 doi:10.1029/2020GC008915.
- 1247 Toni, T., Welch D., Strelkowa, N., Ipsen, A., and Stumpf, M.P.H., 2009, Approximate Bayesian
1248 computation scheme for parameter inference and model selection in dynamical systems,
1249 *Journal of the Royal Society Interface*, v. 6, p. 187-202, doi:10.1098/rsif.2008.0172.
- 1250 Valla, P.G., van der Beek, P.A., and Lague, D., 2010, Fluvial incision into bedrock: Insights
1251 from morphometric analysis and numerical modeling of gorges incising glacial hanging
1252 valleys (Western Alps, France), *Journal of Geophysical Research: Earth Surface*, v. 115,
1253 no. F2, doi:10.1029/2008JF001079.
- 1254 Wynn, R.B., Weaver, P.P.E., Masson, D.G., and Stow, D.A.V., 2002, Turbidite depositional
1255 architecture across three interconnected deep-water basins on the north-west African
1256 Margin, *Sedimentology*, v. 49, no. 4, p. 669-695, doi:10.1046/j.1365-3091.2002.00471.x.
- 1257 Yanites, B.J., Becker, J.K., Madritsch, H., Schnellmann, M., and Ehlers, T.A., 2018, Lithologic
1258 effects on landscape response to base level changes: A modeling study in the context of the
1259 Eastern Jura Mountains, Switzerland, *Journal of Geophysical Research: Earth Surface*, v.
1260 122, p. 2196—2222, doi:10.1002/2016JF004101.
- 1261 Yuan, X.P., Braun, J., Guerit, L., Simon, B., Bovy, B., Rouby, D., Robin, C., and Jiao, R., 2019a,
1262 Linking continental erosion to marine sediment transport and deposition: A new implicit

- 1263 and $O(N)$ method for inverse analysis, *Earth and Planetary Science Letters*, v. 524,
1264 doi:10.1016/j.epsl.2019.115728.
- 1265 Yuan, X.P., Braun, J., Guerit, L., Rouby, D., and Cordonnier, G., 2019b, A new efficient method
1266 to solve the stream power law model taking into account sediment deposition, *Journal of*
1267 *Geophysical Research: Earth Surface*, v. 124, p. 1346—1365, doi:10.1029/2018JF004867.
- 1268 Yuan, X.P., Guerit, L., Braun, J., Rouby, D., and Shobe, C.M., 2022, Thickness of fluvial
1269 deposits records climate oscillations, *Journal of Geophysical Research: Solid Earth*, v. 127,
1270 no. 4, doi:10.1029/2021JB023510.
- 1271 Zhang, J., Sylvester, Z., and Covault, J., 2020, How do basin margins record long-term tectonic
1272 and climatic changes? *Geology*, v. 48, no. 9, p. 893—897, doi:10.1130/G47498.1.
- 1273 Zhang, J., Flaig, P., Wartes, M., Aschoff, J., and Shuster, M., 2021, Integrating stratigraphic
1274 modelling, inversion analysis, and shelf-margin records to guide provenance analysis: An
1275 example from the Cretaceous Colville Basin, Arctic Alaska, *Basin Research*, v. 33, no. 3,
1276 p. 1954-1966, doi:10.1111/bre.12543.